JGR Space Physics

RESEARCH ARTICLE

10.1029/2022JA030853

Key Points:

- We propose an approach to estimate contributions of nonlinear resonant interactions in long-term electron flux dynamics
- We provide rescaling factors of diffusion rates accounting for the contribution of nonlinear electron interactions
- Nonlinear interactions may speed up electron acceleration by a factor of ×1.5–2 during disturbed periods

Supporting Information:

Supporting Information may be found in the online version of this article.

Correspondence to:

A. V. Artemyev,
aartemyev@igpp.ucla.edu

Citation:

Artemyev, A. V., Mourenas, D., Zhang, X.-J., & Vainchtein, D. (2022). On the incorporation of nonlinear resonant wave-particle interactions into radiation belt models. *Journal of Geophysical Research: Space Physics*, *127*, e2022JA030853. https://doi.org/10.1029/2022JA030853

Received 16 JUL 2022
Accepted 4 SEP 2022

On the Incorporation of Nonlinear Resonant Wave-Particle Interactions Into Radiation Belt Models

A. V. Artemyev[1], D. Mourenas[2,3], X.-J. Zhang[1], and D. Vainchtein[4]

[1]Department of Earth, Planetary, and Space Sciences, University of California, Los Angeles, CA, USA, [2]CEA, DAM, DIF, Arpajon, France, [3]Laboratoire Matière en Conditions Extrêmes, Paris-Saclay University, CEA, Bruyères-le-Châtel, France, [4]Nyheim Plasma Institute, Drexel University, Camden, NJ, USA

Abstract Wave-particle resonant interaction is a key process controlling energetic electron flux dynamics in the Earth's radiation belts. All existing radiation belt codes are Fokker-Planck models relying on the quasi-linear diffusion theory to describe the impact of wave-particle interactions. However, in the outer radiation belt, spacecraft often detect waves sufficiently intense to interact resonantly with electrons in the nonlinear regime. In this study, we propose an approach for estimating and including the contribution of such nonlinear resonant interactions into diffusion-based radiation belt models. We consider electron resonances with whistler-mode wave-packets responsible for injected plasma sheet (~100 keV) electron acceleration to relativistic energies and/or for their precipitation into the atmosphere. Using statistics of chorus wave-packet amplitudes and sizes (number of wave periods within one packet), we provide a rescaling factor for quasi-linear diffusion rates, that accounts for the contribution of nonlinear interactions in long-term electron flux dynamics. Such nonlinear effects may speed up 0.1–1 MeV electron diffusive acceleration by a factor of ×1.5–2 during disturbed periods. We discuss further applications of the proposed approach and the importance of nonlinear resonant interactions for long-term radiation belt dynamics.

1. Introduction

The radiation belt dynamics is traditionally modeled within the quasi-linear approach (Andronov & Trakhtengerts, 1964; Kennel & Petschek, 1966) based on a Fokker-Planck diffusion equation for the description of electron interactions with whistler-mode chorus waves. The long-term dynamics of relativistic electron fluxes observed by various spacecraft have been relatively well reproduced by such Fokker-Planck codes during multiple time intervals, lending credence to the reliability of this approach (e.g., see Allison & Shprits, 2020; Drozdov et al., 2015; Glauert et al., 2018; Li et al., 2014; Ma et al., 2018; Su et al., 2016; Thorne et al., 2013; Tu et al., 2014). The wave-driven electron diffusion rates in the Fokker-Plank equation are evaluated under the assumptions of weak wave intensity (Kennel & Engelmann, 1966; Lyons & Williams, 1984; Vedenov et al., 1962) and broadband wave spectrum usually required for the application of the quasi-linear approach (Shapiro & Sagdeev, 1997). The latter requirement can be relaxed in the inhomogeneous magnetic field of the Earth dipole (Karpman, 1974; Le Queau & Roux, 1987), and quasi-linear diffusion rates can be evaluated even for monochromatic waves (Albert, 2010; Karpman & Shklyar, 1977; Shklyar, 2021). Therefore, the main unresolved question for a safe application of the Fokker-Plank equation is posed by multiple observations of very intense waves that will likely interact with electrons nonlinearly (see discussion in Albert et al., 2013; Artemyev, Neishtadt, Vainchtein, et al., 2018; Li & Hudson, 2019, and references therein).

Besides nonlinear electron resonances with intense electromagnetic ion cyclotron waves (e.g., Albert & Bortnik, 2009; Grach & Demekhov, 2020; Kubota et al., 2015; Omura & Zhao, 2012) and ultra-low-frequency waves (e.g., Li et al., 2018,), the observed intensity of whistler-mode waves often exceeds the threshold for nonlinear resonant interactions (e.g., Agapitov et al., 2014; Zhang et al., 2018, 2019). Such intense whistler-mode chorus waves may very quickly accelerate electrons (Agapitov et al., 2015; Demekhov et al., 2006; Gan, Li, Ma, Artemyev, & Albert, 2020; Katoh & Omura, 2007; Omura et al., 2007) or scatter them into the loss-cone (Breneman et al., 2017; Chen et al., 2019,; Miyoshi et al., 2021; Zhang, Artemyev, et al., 2022). Modeling of nonlinear wave-particle interactions, however, is based either on short test particle runs (e.g., Allanson et al., 2020; An et al., 2022; Artemyev et al., 2012; Bortnik et al., 2008; Katoh et al., 2008; Tsai et al., 2022; Zhang, Mourenas, et al., 2020) or on sophisticated generalizations of the Fokker-Planck equation (e.g., Artemyev, Neishtadt, Vasiliev, & Mourenas, 2018; Artemyev, Neishtadt, Vasiliev, Zhang, et al., 2021; Furuya et al., 2008;

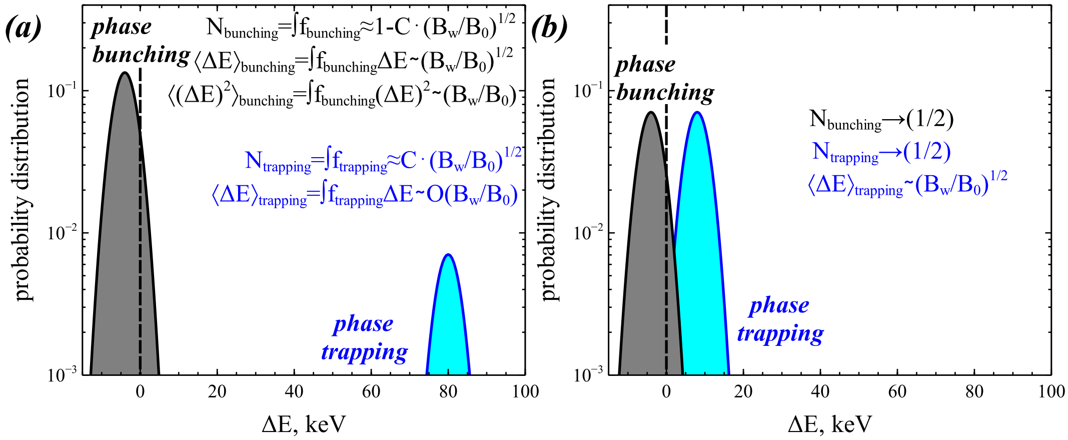

Figure 1. Schematic of distributions of energy changes in a particle ensemble (with the same initial energy/pitch-angles) after a single resonant interaction with (a) intense highly-coherent whistler-mode waves and (b) intense weakly coherent whistler-mode waves. The distribution shown in (a) includes the phase bunched population (gray) and the phase trapped population (blue). The gray population contains most of the particles and has a reduced energy E with $\langle \Delta E\rangle < 0$ proportional to $(B_w/B_0)^{1/2}$ (B_w is the wave amplitude and B_0 the background magnetic field at the latitude of resonance), whereas the blue population contains only a fraction $\sim (B_w/B_0)^{1/2}$ of the resonant particles and is increased in energy by $\langle \Delta E\rangle$ of the order of the initial E. The distribution shown in (b) contains the same two populations, but the phase trapped population is increased to almost half of the total number of resonant particles (with a corresponding decrease of the phase bunched population). Due to the low coherence of the wave, trapped electrons are more quickly released from resonance, with a smaller energy gain (An et al., 2022; Gan et al., 2022; Mourenas et al., 2018; Tao et al., 2013). This decreases $\langle \Delta E\rangle$ and makes it proportional to $(B_w/B_0)^{\kappa}$ with κ depending on the interplay of wave coherence and wave intensity (Artemyev, Neishtadt, Vasiliev, & Mourenas, 2021). For intense short wave-packets $\kappa \sim 1/2$, that is, the average energy changes due to trapping and bunching are comparable, whereas the number of trapped particles becomes similar to the number of phase bunched particles (e.g., Zhang, Agapitov, et al., 2020).

Hsieh & Omura, 2017; Omura et al., 2015), which cannot be straightforwardly incorporated into the existing diffusive models of the radiation belts. A more practicable approach for such an incorporation into existing radiation belt codes would consist in rescaling the quasi-linear diffusion rates to account for the additional contribution of nonlinear interactions in the long-term dynamics of electron fluxes, as first suggested by Artemyev, Neishtadt, Vasiliev, and Mourenas (2021).

There are two good reasons for expecting that such a rescaling will be possible. First, nonlinear interactions of intense waves with electrons are not rare (e.g., Cattell et al., 2008; Cully et al., 2008; Tyler et al., 2019; Wilson et al., 2011; Zhang et al., 2019), but still sporadic and transient phenomena. Therefore, short intervals of rapid electron flux dynamics due to nonlinear interactions are mixed with much longer intervals of more common diffusive dynamics. Such transient bursts of intense waves shall lead to bursty electron precipitations (e.g., Breneman et al., 2017; Chen et al., 2021, 2022; Miyoshi et al., 2020; Tsai et al., 2022; Zhang, Artemyev, et al., 2022), but their contribution to equatorial flux dynamics may be well hidden by the diffusion, which smooths electron phase space density gradients created by nonlinear interactions. Second, most of the observed intense waves are propagating in the form of short wave-packets (e.g., Zhang et al., 2018; Zhang et al., 2021) with strong modulation of wave characteristics within each packets (e.g., Nunn et al., 2021; Santolík et al., 2014; Zhang, Agapitov, et al., 2020; Zhang, Mourenas, et al., 2020). Such modulation is known to reduce the efficiency of nonlinear resonant interactions and to reduce the net effect of such nonlinear interactions to a nearly diffusive one, albeit stronger in magnitude (Allanson et al., 2021; An et al., 2022; Gan, Li, Ma, Albert, et al., 2020; Gan et al., 2022; Mourenas et al., 2018; Tao et al., 2013; Zhang, Agapitov, et al., 2020). Therefore, ignoring the short-lived effects of fast acceleration (e.g., Agapitov et al., 2015; Demekhov et al., 2009; Gan, Li, Ma, Artemyev, & Albert, 2020; Hsieh et al., 2020, 2022) or fast scattering into the loss-cone (e.g., Chen et al., 2022; Zhang, Artemyev, et al., 2022) of small fractions of the total electron population, the long-term effect of nonlinear interactions may be reduced to a diffusion that would be faster or slower than the classical quasi-linear diffusion (Allanson et al., 2022; Artemyev, Neishtadt, Vasiliev, & Mourenas, 2021; Shklyar, 2021). Figure 1 illustrates this approach by showing a schematic of probability distribution functions of electron energy changes due to a single resonant interaction with waves of different amplitudes (see examples of such distributions in Tao et al., 2013; Zhang, Agapitov, et al., 2020; An et al., 2022; Gan et al., 2022).

In this study, we propose an approach for the derivation of the relation between nonlinear and quasi-linear generalized diffusion rates $D_{\mathrm{NL}}/D_{\mathrm{QL}}$, where D_{NL} is defined as the effective diffusion rate that would result in the same time-scale of diffusive evolution of electron fluxes as the corresponding time-scale of evolution due to nonlinear interactions. The ratio $D_{\mathrm{NL}}/D_{\mathrm{QL}}$ depends on two main system parameters: wave intensity, B_w^2, and the parameter β controlling the wave-packet amplitude modulation (Artemyev, Neishtadt, Vasiliev, & Mourenas, 2021). The dependence of $D_{\mathrm{NL}}/D_{\mathrm{QL}}$ on B_w^2 underlines that D_{NL} depends on wave intensity in a nonlinear manner. The parameter β can be introduced as a wave-packet length measured in wavelength, or as a wave-packet duration measured in wave periods.

The paper is organized as follows. In Section 2 we describe the basic properties of electron nonlinear resonant interactions with field-aligned whistler-mode waves. We also relate the wave-packet size β with the characteristics of such interactions. In Section 3, we describe an approach for evaluating D_{NL} for fixed wave characteristics. In Section 4, we show D_{NL} for three energy/pitch-angle ranges of crucial importance in the radiation belts: ∼1 MeV electrons with small pitch-angles and ∼100–300 keV electrons with large pitch-angles. In Section 5, we provide the corresponding rescaling factor $\langle R\rangle = \langle D_{\mathrm{NL}}\rangle/\langle D_{\mathrm{QL}}\rangle$ of quasi-linear diffusion rates D_{QL}, averaged over measured statistical distributions of the main wave characteristics $\left(B_w^2, \beta\right)$. In Section 6, we discuss the obtained results and their applications for radiation belt models.

2. Basic Characteristics of Nonlinear Resonant Interaction

The resonant interaction of a relativistic electron (rest mass is m_e, charge is $-e$) with a field-aligned propagating whistler-mode wave can be described by the Hamiltonian (e.g., Albert et al., 2013; Vainchtein et al., 2018):

$$H = m_e c^2 \gamma + \sqrt{\frac{2 I_x \Omega_0}{m_e c^2}}\frac{e B_w}{k\gamma}\cos(\phi + \psi), \quad \gamma = \sqrt{1 + \left(\frac{p_\parallel}{m_e c}\right)^2 + \frac{2 I_x \Omega_0}{m_e c^2}} \tag{1}$$

where $(s, p_\parallel)$ are conjugated field-aligned coordinate and momentum, (ψ, I_x) are conjugated gyrophase and magnetic moment, $\Omega_0 = eB_0(\lambda)/m_e c$ with $B_0(\lambda)$ is the dipole magnetic field as a function of magnetic latitude λ given by equation $ds/d\lambda = LR_E\sqrt{1+3\sin^2\lambda}\cos\lambda$, $k = k(\lambda)$ is the wave number given by whistler-mode wave dispersion relation for a cold plasma (Stix, 1962), $B_w(\lambda)$ is the wave amplitude depending on magnetic latitude, ϕ is the wave phase determined by wave frequency $\omega = -\partial\phi/\partial t$ and $k = \partial\phi/\partial s$. The magnetic moment I_x relates to the local electron pitch-angle α and to the equatorial pitch-angle α_{eq} as: $I_x = m_e c^2(\gamma^2 - 1)\sin^2\alpha/\Omega_0(s) = m_e c^2(\gamma^2 - 1)\sin^2\alpha_{\mathrm{eq}}/\Omega_0(0)$. To set $B_w(\lambda) = B_w(0)\cdot\tanh\left(\lambda^2/\delta\lambda_1^2\right)\exp\left(-\lambda^2/\delta\lambda_2^2\right)$ we consider a classical scenario of wave generation around the equatorial plane (e.g., Katoh & Omura, 2013; Katoh & Omura, 2016; Tao et al., 2017, and references therein) with damping at high latitudes (see, e.g., empirical models of $B_w(\lambda)$ in Agapitov et al., 2018). We use $\delta\lambda_1 = 2°$ and $\delta\lambda_2 = 20°$, that fit the typical $B_w(\lambda)$ distribution for intense (observed during geomagnetically active condition) waves (Agapitov et al., 2013, 2018; Wang et al., 2019).

For whistler-mode waves $kR_E L \gg 1$, $\omega R_E L/c \gg 1$, $\Omega_0 R_E L/c \gg 1$, and thus, wave phase ϕ changes much faster than the time-scale of electron bouncing along geomagnetic field lines. This separation of time-scales allows to expand the Hamiltonian Equation 1 around the resonance $\dot{\phi} + \dot{\psi} = (kp_\parallel/\gamma m_e) - \omega + \Omega_0/\gamma = 0$ as (e.g., Artemyev, Neishtadt, Vasiliev, & Mourenas, 2018; Vainchtein et al., 2018):

$$H_\zeta = \frac{1}{2} g P_\zeta^2 + \mathrm{A}\zeta + \mathrm{B}\cos\zeta \tag{2}$$

where $\zeta = \phi + \psi$, P_ζ is the momentum conjugated to ζ (i.e., $P_\zeta = 0$ is the resonance), g, A, and B are functions of field-aligned coordinate s and momentum $P_\parallel = p_\parallel + kI_x$, and $(s, P_\parallel)$ are given by the combination of the resonant condition $(kp_\parallel/\gamma m_e) - \omega + \Omega_0/\gamma = 0$ and the conservation law $m_e c^2\gamma - I_x\omega = \mathrm{const}$. Functions $B \sim B_w$ and $A \sim \partial\Omega_0/\partial s$ describe the effects of wave field and magnetic field inhomogeneity on electron dynamics at resonance. The competition of these effects determines the electron dynamics, including phase bunching and phase trapping (see expressions for A, B in, e.g., Artemyev, Neishtadt, Vasiliev, & Mourenas, 2018; Vainchtein et al., 2018). The

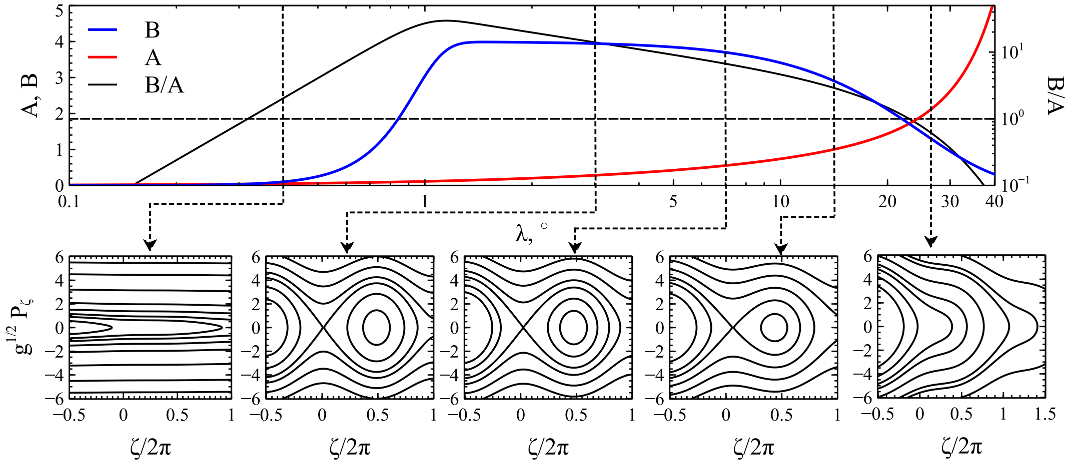

Figure 2. (top) Profiles of coefficients A, B, and ratio B/A along magnetic latitude for typical parameters of wave-particle interaction. The wave intensity (controlling B) increases from zero at the equator to a maximum value around a few degrees off-equator and then decreases to zero at high latitudes. The coefficient A is proportional to $\partial\Omega_0/\partial s$: it is zero at the equator and increases at higher latitudes. (bottom) Phase portraits of Hamiltonian Equation 2 for five B/A ratios (at five latitudes).

analysis of Hamiltonian Equation 2 is often replaced by an analysis of the analogous equation $\ddot{\zeta} + \tilde{\mathrm{A}} - \tilde{\mathrm{B}}\sin\zeta = 0$ (e.g., Karpman et al., 1974; Karpman, Istomin, & Shklyar, 1975; Nunn, 1974; Omura et al., 2007; Shklyar, 1981).

Although Hamiltonian Equation 1 describes electron motion in 4D phase space of $(s, p_\parallel, I_x, \psi)$ with the time dependence, the system's dimensionality can be significantly reduced for electron interaction with a monochromatic wave (when $\partial\phi/\partial t = \mathrm{const}$). In the absence of waves, the conservation of energy and magnetic moment I_x guarantees the conservation of equatorial pitch-angle α_{eq} and, thus, the unperturbed system is fully described by two constants (γ, I_x) or $(\gamma, \alpha_{\mathrm{eq}})$. The resonant condition $(kp_\parallel/\gamma m_e) - \omega + \Omega_0/\gamma = 0$ determines the resonant position in $(s, p_\parallel)$ space as a function of (γ, I_x). For a monochromatic wave, there is an integral of particle energy in the wave reference frame, $m_e c^2\gamma - \omega I_x = \mathrm{const}$, and this integral removes $p_\parallel$ from the consideration, that is, for fixed ω the resonance condition gives $s = s_R(\gamma)$. This equation can be rewritten as $\gamma = \gamma_R(s) = \gamma_R(\lambda)$, where γ_R is the energy in the resonance (γ with $p_\parallel$ is defined by resonance condition and I_x is defined by $m_e c^2\gamma - \omega I_x = \mathrm{const}$). Thus, a fixed ω determines a curve $m_e c^2\gamma - \omega I_x = \mathrm{const}$ in the (γ, I_x) or $(\gamma, \alpha_{\mathrm{eq}})$ space, and each position on this curve corresponds to some latitudes of resonance λ_R. Resonant wave-particle interactions move electrons along such curves (that are defined by the value of constant $m_e c^2\gamma - \omega I_x = \mathrm{const}$), and there is a single-valued relation between the electron position on this curve and the resonant latitude λ_R. As a result, coefficients g, A, B in Hamiltonian Equation 2 are functions of λ_R only or, equivalently, of γ_R. An additional result of the conservation of $m_e c^2\gamma - \omega I_x = \mathrm{const}$ is that the energy change in the resonance is proportional to the I_x change, $\Delta\gamma = \omega\Delta I_x/m_e c^2$, and this relation provides the pitch-angle change $\Delta\alpha_{\mathrm{eq}}$ as a function of the energy change $\Delta\gamma$.

Figure 2 shows the phase portraits of Hamiltonian Equation 2 for a typical wave amplitude distribution along a geomagnetic field line. The resonance condition $p_\parallel = m_e(\gamma\omega - \Omega_0)/k$ shows that not-too-energetic resonant electrons ($\gamma < \Omega_0/\omega$) are moving in the opposite direction to the wave propagation direction, that is, waves are generated at the equator and propagate toward high latitudes and resonant electrons are moving from high latitudes to the equator.

Electrons interacting resonantly with waves at high latitudes will see the phase portrait with $|\mathrm{A}| > |\mathrm{B}|$ due to the large background magnetic field gradient ($\mathrm{A} \sim \partial\Omega_0/\partial s$) and small wave amplitudes ($\mathrm{B} \sim B_w$) there. All electrons with the same initial energy γ and pitch-angle α_{eq} will experience a change of magnetic moment $\Delta I_x = \Delta I_x(\gamma, \alpha_{\mathrm{eq}}, \zeta_0)$, where ζ_0 determines the initial electron phase ζ (and can be recalculated to the electron phase in the resonance ζ_R). The average magnetic moment change $\langle\Delta I_x\rangle_{\zeta_0}$ is equal to zero, and there is only diffusion $\langle(\Delta I_x)^2\rangle \neq 0$. This diffusion rate $\langle(\Delta I_x)^2\rangle$ can be evaluated analytically (Karpman & Shklyar, 1977) and has been shown to be equal to quasi-linear diffusion coefficients (Albert, 2010) for $|\mathrm{A}| \gg |\mathrm{B}|$ with $\langle(\Delta I_x)^2\rangle \propto B_w^2$.

Electrons resonating with waves at intermediate latitudes will see a phase portrait with $|\mathrm{A}| < |\mathrm{B}|$ (if wave intensity is sufficiently high). This phase portrait contains a region with closed trajectories oscillating around the reso-

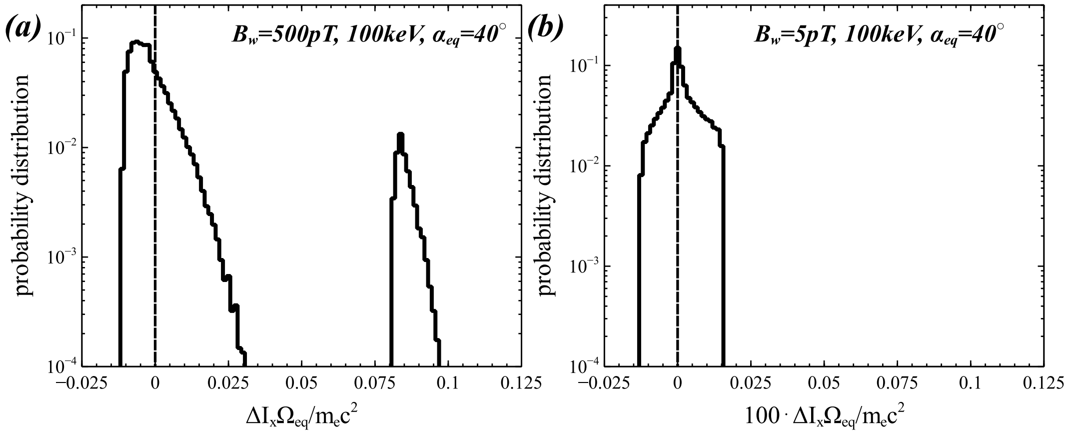

Figure 3. Two distributions of ΔI_x changes obtained by integrating an ensemble of trajectories given by Hamiltonian Equation 1. All particles in each of these two ensembles have the same initial energy and pitch-angle and resonate with the wave only once. Panel (a) shows results for a very intense wave (|B/A| > 1), and panel (b) show results for a wave with $a \times 1/100$ weaker amplitude (|B/A| < 1). Note that to show these two distributions within the same ΔI_x range, we have multiplied ΔI_x by 100 in panel (b).

nance $P_\zeta = 0$, that is, phase trapped trajectories. The separatrix demarcates the phase space regions with such trapped trajectories and other trajectories crossing the resonance $P_\zeta = 0$ only once. The presence of a region of finite (non-zero) area $S = \oint P_\zeta d\zeta$ surrounded by the separatrix changes the character of electron resonant interaction with waves. Electrons meeting the resonance $P_\zeta = 0$ only once experience *phase bunching*, and electrons oscillating around the resonance $P_\zeta = 0$ along the closed orbits are *phase trapped*.

To explain these resonance effects, let us consider an ensemble of N electrons with the same initial energy and I_x (same initial α_{eq}), but with different random ζ_0. All these electrons have the same latitude of resonance and for them the Hamiltonian Equation 2 is identical. Interaction with the wave results in I_x change, and Figure 3 shows the schematics of ΔI_x distributions for |A| < |B| (a) and |A| > |B| (b). Note that due to the relation $\omega \Delta I_x / m_e c^2 = \Delta\gamma$, the distributions of ΔI_x and $\Delta\gamma$ are the same. In the absence of nonlinear resonant effects (|A| > |B|), the distribution $F(\Delta I_x)$ is symmetric relative to $\Delta I_x = 0$ and the dispersion $\langle (\Delta I_x)^2 \rangle \propto (B_w/B_0)^2$ for sufficiently small |B|/|A| (e.g., Albert, 2001, 2010; Karpman & Shklyar, 1977). In the presence of nonlinear resonant effects (|A| < |B|), the distribution $F(\Delta I_x)$ consists of two well separated populations. The most representative population contains almost all particles, $\sim N$, and have a finite $\langle \Delta I_x \rangle \propto (B_w/B_0)^{1/2}$ for sufficiently large |B|/|A| (e.g., Albert, 2000; Artemyev et al., 2014; Shklyar, 2011). The dispersion of this population is $\langle (\Delta I_x)^2 \rangle \to (B_w/B_0)^\kappa$ with $\kappa \to 1$ for sufficiently large |B|/|A| (e.g., Karpman, Istomin, & Shklyar, 1975; Karpman & Shklyar, 1977). Such finite $\langle (\Delta I_x) \rangle$ means that all particles are shifted in I_x (in energy). This effect is called *phase bunching* (e.g., Demekhov et al., 2006; Omura et al., 1991; Shklyar & Matsumoto, 2009). A much smaller electron population contains only a fraction $(B_w/B_0)^{1/2}$ of all resonant particles, $\sim (B_w/B_0)^{1/2} N$, and this fraction goes to zero if at the latitude of resonance the area S decreases along the electron trajectories (e.g., Artemyev et al., 2015; Karpman, Istomin, & Shkliar, 1975; Neishtadt, 1975; Shklyar, 1981). This population is characterized by a finite $\langle \Delta I_x \rangle \sim O(B_w/B_0)$. Such a large I_x (energy γ) change is due to *phase trapping* (e.g., Artemyev et al., 2015; Omura et al., 2007; Vainchtein et al., 2018). The dispersion of the entire $F(\Delta I_x)$ distribution is about

$$\left\langle (\Delta I_x)^2 \right\rangle \approx \langle \Delta I_x \rangle^2_{bunching} \frac{N_{bunching}}{N} + \langle \Delta I_x \rangle^2_{trapping} \frac{N_{trapping}}{N} \sim \left(\frac{B_w}{B_0}\right) \cdot O\left(\frac{B_w}{B_0}\right) + O\left(\frac{B_w}{B_0}\right) \cdot \left(\frac{B_w}{B_0}\right)^{1/2} \sim \left(\frac{B_w}{B_0}\right)^{1/2}$$

To evaluate all averaged system characteristics ($\langle \Delta I_x \rangle_{bunching}$, $\langle \Delta I_x \rangle_{trapping}$, and N_{trapping}), we need only one function: $S = S(\lambda)$, written as $S = S(I_x)$:

$$S = \oint P_\zeta d\zeta = \frac{2}{\sqrt{g}} \int_{\zeta_-}^{\zeta_+} \sqrt{\mathrm{A}(\zeta_+ - \zeta) + \mathrm{B}(\cos\zeta_+ - \cos\zeta)}\, d\zeta$$

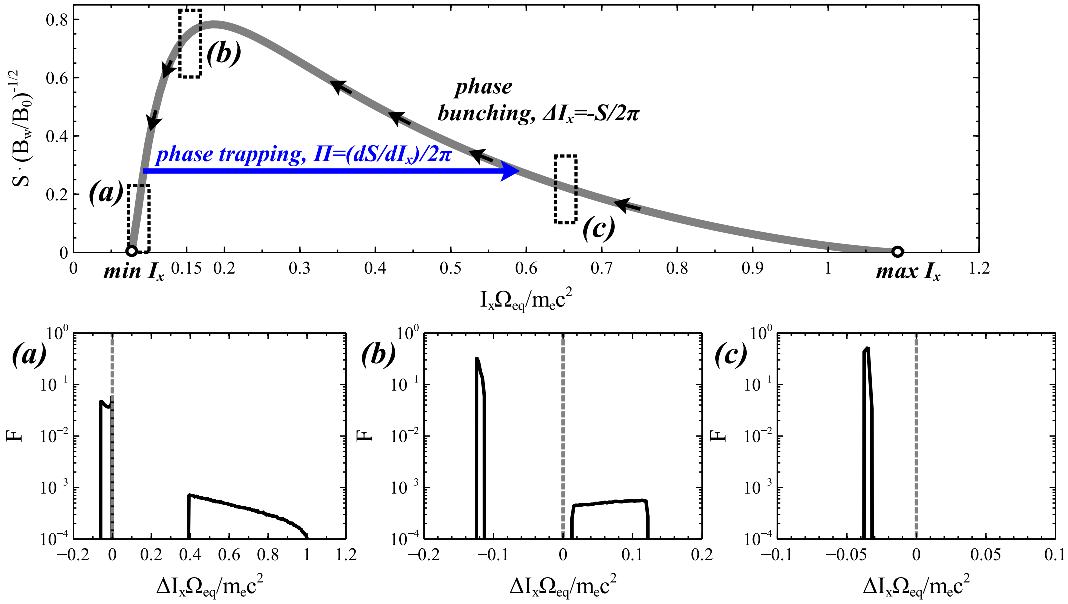

Figure 4. (top) Model $S(I_x)$ profile and scheme of trapped and phase bunched particle motion along I_x. (bottom) Distributions of ΔI_x obtained with map (5) for three small I_x ranges marked by (a), (b), and (c) in the top panel.

where $\zeta_- = \arccos{(A/B)}$, see Figure 2 and Artemyev, Neishtadt, Vasiliev, and Mourenas (2018).

For an initial I_x, the phase bunching results in $\langle \Delta I_x \rangle_{bunching} = -S\,(I_x)\,/2\pi$ and the trapping probability $\Pi = N_{\text{trapping}}/N = (\mathrm{d}S/\mathrm{d}I_x)/2\pi$ (Cary et al., 1986; Neishtadt, 1975; Shklyar, 1981). The change of $\langle \Delta I_x \rangle_{trapping}$ is determined as $I_{x,\text{final}} - I_x$ where $S(I_{x,\text{final}}) = S(I_x)$, and $\mathrm{d}S/\mathrm{d}I_x < 0$ at $I_{x,\text{final}}$ (e.g., Artemyev et al., 2015). Therefore, there is a simple *geometrical* interpretation of nonlinear wave-particle interactions: many particles drift in I_x space to smaller I_x with the velocity of drift $\langle \Delta I_x \rangle_{bunching}/\tau$, whereas in the I_x range with $\mathrm{d}S/\mathrm{d}I_x > 0$ some particles can be trapped with a probability of trapping Π/τ and transported to larger I_x (see Figures 4a and Artemyev, Neishtadt, Vasiliev, & Mourenas, 2018; Artemyev, Neishtadt, et al., 2016). The typical time-scale τ of this motion is determined as the time between two resonances, and for a single wave resonating with electrons τ is equal to half of the bounce period along geomagnetic field lines. Figure 4 shows a schematic of the $S(I_x)$ profile and the corresponding $F(\Delta I_x)$ distributions. Such a relation between properties of individual electron resonances and the system characteristics, $S(I_x)$, allows us to provide a description of the long-term dynamics of an electron ensemble with multiple nonlinear resonances.

Note that schematics in Figures 2 and 4 are displayed for electrons moving with resonant momentum $p_{\|} = m_e(\gamma\omega - \Omega_{ce})/k < 0$ during the trapping motion. Sufficiently energetic (relativistic) electrons may be accelerated within the trapping to such energies that γ becomes larger than Ω_{ce}/ω, so that such trapped electrons can change their direction of motion and continue to be accelerated for a longer time (a phenomenon called turning acceleration, see Omura et al., 2007; Summers & Omura, 2007). This effect is well described by Hamiltonian system Equation 1, but we do not provide here a schematic illustration of such turning acceleration.

3. Mapping Technique for the Evaluation of D_{NL}

Let us consider the mapping technique for wave-particle resonant interaction. A classical example of such a technique is the Chirikov map (Benkadda et al., 1996; Chirikov, 1979; Khazanov et al., 2013) that describes particle diffusion due to wave-particle interaction. For Hamiltonian Equation 1, this map works as

$$\begin{cases} I_x^{(n+1)} = I_x^{(n)} + \delta I_x\left(I_x^{(n)}\right)\sin\zeta^{(n)} \\ \zeta^{(n+1)} = \zeta^{(n)} + \delta\zeta\left(I_x^{(n+1)}\right) \end{cases} \tag{3}$$

where n is the number of iterations (i.e., time is $t^{(n+1)} = t^{(n)} + \tau$), functions δI_x and $\delta\zeta$ describe the magnitude of I_x change at the resonance and the phase gain between two successive resonances. Since such phase gain $\delta\zeta \sim \omega\tau \gg 1$ for τ about a fraction of the bounce period, ζ can be taken as a random number with a distribution such that the $\sin\zeta$ distribution repeats the properties of $\Delta I_x = I_x^{(n+1)} - I_x^{(n)}$ distributions. Although the ΔI_x distribution can be evaluated numerically (Artemyev et al., 2019; Itin et al., 2000; Lukin et al., 2021), this is computationally very expensive for a realistic multi-parameter system. Moreover, we are mostly interested in describing the phase averaged properties of I_x changes and, thus, we can reduce the map Equation 3 to

$$I_x^{(n+1)} = I_x^{(n)} + \sqrt{\left\langle (\Delta I_x)^2 \right\rangle} \cdot \left(2\xi^{(n)} - 1\right) \tag{4}$$

where ξ is a random value with a uniform distribution in [0, 1] and $\langle(\Delta I_x)^2\rangle \propto (B_w/B_0)^2$ describes the dispersion of I_x changes in the system with a small wave intensity, |A| > |B|.

For a system with nonlinear resonant interactions (|A| < |B|), the analog of map (3) has been derived and verified in Artemyev et al. (2020b); Artemyev et al. (2020a):

$$I_x^{(n+1)} = I_x^{(n)} + \begin{cases} \langle \Delta I_x \rangle_{bunching}, & \xi^{(n)} \in [\Pi, 1] \\ \langle \Delta I_x \rangle_{trapping}, & \xi^{(n)} \in [0, \Pi) \end{cases} \tag{5}$$

where ξ is a random value with a uniform distribution in [0, 1] and all system parameters ($\langle \Delta I_x \rangle_{bunching}$, $\langle \Delta I_x \rangle_{trapping}$, Π) are described by the $S(I_x)$ profile. Map Equation 5 has been shown to describe well the long-term dynamics of an electron ensemble in different systems with nonlinear interactions (see Artemyev, Neishtadt, Vasiliev, Zhang, et al., 2021; Artemyev et al., 2022; Zhang, Artemyev, et al., 2022).

Figure 5a shows different examples of individual electron trajectories described by the maps (4) and (5) for model $S(I_x)$ and $\langle(\Delta I_x)^2\rangle(I_x)$ functions. There are random walks for map Equation 4, and a combination of bunching (drift) and trapping (rare large jumps) for map Equation 5. If we set an ensemble of N particles with initial uniform I_x distribution along the range of nonzero $\langle(\Delta I_x)^2\rangle$ (i.e., the range of resonant I_x for fixed ω and $m_e c^2\gamma - \omega I_x = \text{const}$) and trace them for a sufficiently long time (during a sufficiently large number of iterations, $n \gg 1$), we can calculate the dynamics of the distribution variance

$$\mathcal{M}_2(n) = \frac{1}{N}\sum_{l=0}^{N}\left(I_x(n) - I_x(0)\right)^2 - \mathcal{M}_1^2(n), \quad \mathcal{M}_1(n) = \frac{1}{N}\sum_{l=0}^{N}\left(I_x(n) - I_x(0)\right)$$

Figure 5b shows that $\mathcal{M}_2 \propto n$ for both maps (see discussion in Artemyev, Neishtadt, Vasiliev, & Mourenas, 2021). The proportionality coefficient $d\mathcal{M}_2/dn$ can be interpreted as a generalized (averaged over the energy/pitch-angle range of resonant interactions along $m_e c^2\gamma - \omega I_x = \text{const}$ curves) diffusion rate. For map (4), we have $D_{QL} = d\mathcal{M}_2/dn \sim (B_w/B_0)^2$, and for map (5) we have $D_{NL} = d\mathcal{M}_2/dn \sim (B_w/B_0)^{1/2}$. Previous numerical simulations have shown that the transition from quasi-linear diffusion to nonlinear resonant interactions is characterized by a weaker dependence of the usual electron diffusion rate on B_w/B_0 (e.g., Gan, Li, Ma, Albert, et al., 2020; Tao et al., 2012). This underlines an important difference between quasi-linear diffusion and nonlinear resonant interactions (see more examples in Artemyev, Neishtadt, Vasiliev, & Mourenas, 2021). However, the usual diffusion rate only includes weak quasi-linear scatterings, whereas the effective rate $D_{\rm NL}$ incorporates the stronger effects of nonlinear interactions. Hereafter, we use the mapping technique to quantify the ratio $D_{\rm NL}/D_{\rm QL}$ for realistic system parameters.

4. $D_{\rm NL}$ for Realistic Wave Characteristics

The wave amplitude (more precisely, the wave amplitude profile along geomagnetic field lines) determines the $S(I_x)$ profile and, thus, controls all characteristics of wave-particle nonlinear interactions for a fixed background field. However, such a single-parameter, B_w/B_0, approach works only under the approximation of plane waves (i.e., for sufficiently long wave-packets). Spacecraft observations show that intense waves rarely propagate in the form of long wave-packets and that wave-packets most often contain only $\beta \leq 10$ wave periods (Zhang et al., 2019). Recent comparisons of wave packet statistics and different models of whistler-mode (chorus) wave

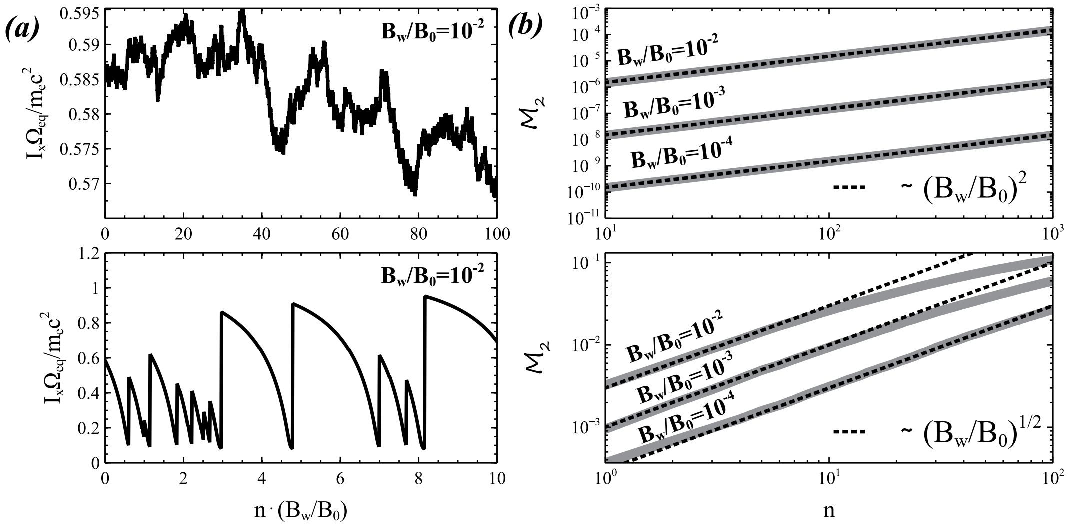

Figure 5. (a) Examples of $I_x(n)$ profiles obtained with map (4) describing diffusion (top) and with map (5) describing nonlinear resonant interactions (bottom). For map (5) we use the model profile $S(I_x)$ shown in Figure 4 (top), and for map (4) we use $\langle(\Delta I_x)^2\rangle = S^2(I_x)$. (b) $\mathcal{M}_2(n)$ profiles for the ensemble of trajectories integrated with map (4) describing diffusion (top) and with map (5) describing nonlinear resonant interactions (bottom). Black dotted lines show fits with $\mathcal{M}_2 \sim (B_w/B_0)^2$ (top) and $\mathcal{M}_2 \sim (B_w/B_0)^{1/2}$ (bottom).

generation (Zhang et al., 2021) have confirmed that the formation of short packets $\beta \leq 10$ naturally results from nonlinear mechanisms of wave generation. Therefore, the second important parameter controlling the nonlinear wave-particle interactions is the finite wave-packet length (or duration) measured in wave periods, β. The wave-packet length defines the maximum possible duration of trapping in a given packet, and the corresponding acceleration magnitude in the absence of internal phase jumps that may destroy trapping (Zhang, Agapitov, et al., 2020). In addition, electron acceleration by a *train of wave-packets* may be quite effective in case of multiple consecutive trapping (Hiraga & Omura, 2020), but this effect is often reduced by the presence of large and random wave phase jumps between consecutive packets (Zhang, Agapitov, et al., 2020). Below, we shall consider two different types of wave-packet amplitude modulations, such that moderate modulations allow the presence of multiple consecutive trappings whereas strong modulations mostly suppress them. To highlight the importance of β, let us consider the peculiarities of trapped particle dynamics. A trapped particle oscillates within the effective potential of Hamiltonian Equation 1 with the oscillation period (e.g., Karpman et al., 1974; Nunn, 1971; Nunn, 1974)

$$T_{trapping} = \frac{2\pi}{\Omega_{trapping}} \approx \frac{2\pi}{\Omega_0}\left(\sqrt{\frac{2I_x\Omega_0}{m_ec^2}}\,\frac{B_w}{\gamma B_0}\right)^{-1/2}$$

The maximum duration of electron resonant interaction with the wave-packet is determined as

$$T_{\max} = \frac{2\pi}{k}\frac{\beta}{|v_R - v_g|} = 2\pi\beta\left|\omega - \frac{\Omega_0}{\gamma} - k\frac{\partial\omega}{\partial k}\right|^{-1} \approx \frac{2\pi\beta\gamma}{\Omega_0}$$

We use the simplified wave dispersion $\omega = \Omega_0\left(1+(kd_e)^{-2}\right)^{-1}$ for a typical $k \sim 1/d_e$, where d_e is the electron inertial length. During the trapping, electrons make

$$K_{trapping} = \frac{T_{\max}}{T_{trapping}} = \beta\left(\sqrt{\frac{2I_x\Omega_0}{m_ec^2}}\,\frac{\gamma B_w}{B_0}\right)^{1/2} \propto \beta\left(\frac{B_w}{B_0}\right)^{1/2}$$

oscillations, whereas transient electrons cross the resonance within times-scale $\sim T_{\text{trapping}}$. Thus, for $K_{\text{trapping}} \sim 1$, that is, for $\beta \sim (B_0/B_w)^{-1/2}$, there is no significant separation of time-scales spend by transient and trapped electrons in the resonance, and the changes of energies/pitch-angles for these two populations of electrons remain comparable (see more detailed estimates in Artemyev, Neishtadt, Vasiliev, & Mourenas, 2021). Importantly, the

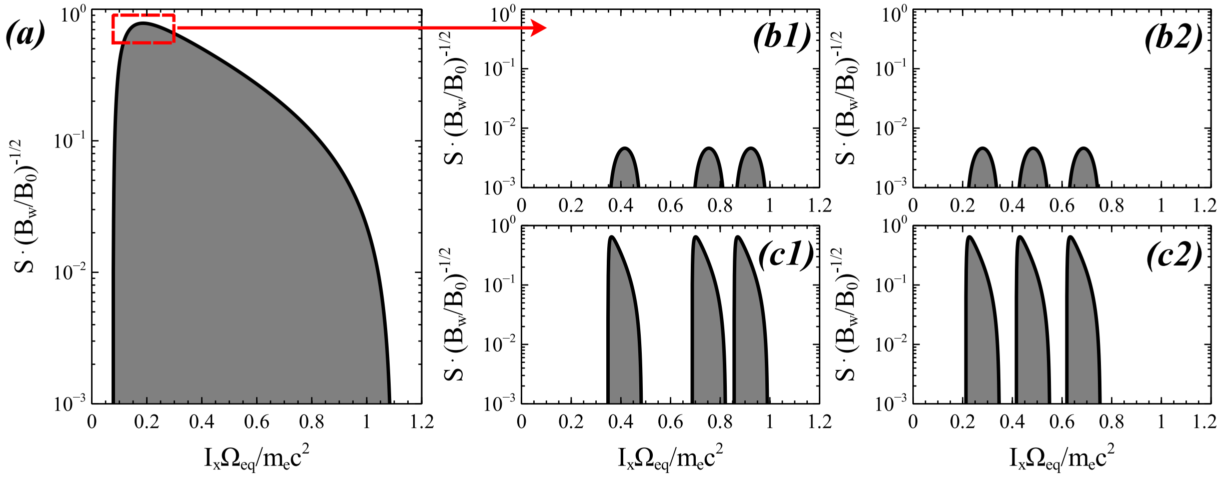

Figure 6. Schematic of system change from the long wave-packet (a) to multiple small (but still above the threshold of nonlinear wave-particle interactions) amplitude wave-packets (b) or to multiple very intense wave-packets (c). In case (b) the S of multiple wave-packets is the top part of S of a single long wave-packet. In case (c) S of multiple wave packets is the same as S of a single long wave-packet, but with the narrowed I_x range. (b1, b2) and (c1, c2) show change with time of S locations for series of wave-packets.

decrease of β not only reduces the efficiency of acceleration of individual trapped electrons, but also changes the probability of trapping. For $\beta \to \infty$ (plane waves) this probability is determined as $\sim dS/dI_x$ with the $S(I_x)$ gradient controlled by the $B_w(\lambda)$ profile along magnetic field lines. For small β, the strongest S gradients occur at the wave-packet edges, and electrons can interact with packet edges at any latitude of resonance. Instead of a geometrical interpretation with a single $S(I_x)$ profile as in Figure 4, we must consider multiple smaller $S(I_x)$ profiles with randomly changing locations on the I_x-axis (see schematic in Figure 6). There are two possible scenarios of wave-particle resonant interaction with small β packets. To describe these scenarios, let us consider a model $S(I_x) = (B_w/B_0)^{1/2}\cdot(I_+ - I_x)^{5/4}(I_x - I_-)^{5/4}/\delta I_0^2$, where $I_\pm$ and δI_0 determine parameters of $S(I_x)$ profile, whereas the factor $(B_w/B_0)^{1/2}$ changes S with wave amplitude in agreement with Hamiltonian Equation 2. For large wave packets $I_\pm$, δI_0 do not vary with B_w/B_0 but depend on the field-aligned profiles of B_w and the background magnetic field (e.g., Artemyev, Neishtadt, Vasiliev, & Mourenas, 2018). As β decreases, the range of resonant I_x shrinks ($I_+ - I_-$ goes down), and δI_0 also changes. In the first scenario, the β decrease results from the decrease of B_w/B_0. In this case $I_\pm$ and δI_0 should start varying with B_w/B_0, and the $S(I_x)$ model, after normalization, will vary with B_w/B_0 like $S(I_x) \propto (B_w/B_0)^{1/2+\kappa}$, with $\kappa \to 5/6$ $\left(S \propto (B_w/B_0)^{4/3}\right)$ for a critically small β value corresponding to $K_{\text{trapping}} \sim 1$ (see corresponding calculations in Artemyev, Neishtadt, Vasiliev, & Mourenas, 2021). This scenario corresponds to the schematic shown in Figures 6a and 6b, with a large single $S(I_x)$ evolving into a series of small $S(I_x)$ as the amplitude decreases. In the second scenario; β does not depend on B_w/B_0, and the small β results in a very strong increase of the probability of trapping, because dS/dI_x goes up with $I_+ - I_-$ going down for fixed B_w/B_0. This scenario corresponds to the schematic shown in Figures 6a and 6c, with a large single $S(I_x)$ evolving into a series of small $S(I_x)$ with fixed amplitude. The fine interplay of B_w and background parameter profiles along magnetic field lines, the small β effect, and probabilities for electrons to interact with waves of different B_w at the same resonant latitude due to the finite wave-packet size, mix these two scenarios in realistic systems. Thus, instead of using a model $S(I_x)$ function for mapping (4), we adopt the approach proposed in Artemyev et al. (2019); Lukin et al. (2021) and numerically calculate $F(\Delta I_x)$ distributions for a wide range of B_w/B_0 and β parameters.

To use numerical calculations of $F(\Delta I_x)$, one must include evaluations of multiple trajectories with the map

$$I_x^{(n+1)} = I_x^{(n)} + \Delta I_x(I_x), \qquad t^{(n+1)} = t^{(n)} + \frac{1}{2}\tau_{bounce}^{(n)}\left(I_x^{(n)}\right) \tag{6}$$

describing ΔI_x changes with the given $F(\Delta I_x)$ under assumption of a single resonant interaction during half of a bounce period. Distributions $F(\Delta I_x, I_x)$ are evaluated for a dense I_x net covering the range of I_x with nonlinear resonant interactions for a fixed $m_ec^2\gamma - \omega I_x$ parameter and fixed system characteristics (ω, L-shell, B_w profile, and β). Using map (5), we evaluate the $\mathcal{M}_2(n)$ function and approximate it by a linear fit, $\mathcal{M}_2 \approx Dn$. The fitting coefficient D determines the diffusion rate (note that an additional fitting with Dt^q gives $q \sim 1$ and confirms that we deal with a diffusive process). For each set of system parameters, we construct a set of distributions for a wide range of peak wave amplitude $B_w \in [B_{w,\min}, B_{w,\max}]$ (henceforth, the peak amplitude of wave-packets is denoted B_w for simplicity). The smallest $B_{w,\min} \sim$ 5pT corresponds to the regime of quasi-linear diffusion, and thus we can consider normalized distributions $\bar{F}\left(\Delta I_x \cdot (B_{w,\max}/B_w)\right)$ and the corresponding fitting coefficients $\bar{D}$ (for a purely diffusive process, this normalization would mean $\bar{D} = (B_{w,\max}/B_w)^2 \cdot D(B_w)$). The ratio $R = \bar{D}(B_w)/\bar{D}(B_{w,\min}) \simeq D_{NL}/D_{QL}$ describes the deviation of the scattering rate from the quasi-linear diffusion rate. This ratio R depends on β and on the parameter describing the depth of the wave amplitude modulation, that is, on the ratio of the minimum and maximum wave field amplitudes inside a packet, min/max. We use a moderate modulation with min/max = 5/100 and a strong modulation with min/max = 7/1000. The stronger modulation corresponds to a more probable electron escape from trapping at the wave-packet edge, and less probable multiple trappings into several consecutive wave-packets (see examples of such multiple trappings in Hiraga & Omura, 2020).

Figure 7a1–7a3 show examples of $C(\Delta I_x)$ cumulative distributions corresponding to $\bar{F}(\Delta I_x)$ for different wave amplitudes B_w, two β values, and two different magnitudes of the wave amplitude modulation inside the packet. Although the range of ΔI_x is comparable for all B_w after normalization, for large β there is a clear transition from $C(\Delta I_x)$ symmetric relative to $\Delta I_x = 0$ for the smallest $B_w \sim B_{w,\min}$ to $C(\Delta I_x)$ having a long tail of large ΔI_x for the largest $B_w \to B_{w,\max}$. For small β, the cumulative distribution $C(\Delta I_x)$ has a less pronounced large ΔI_x population (i.e., for the strong modulation $C(\Delta I_x)$ shows a large ΔI_x population only for $B_w = B_{w,\max}$). This is due to nonlinear trapping destruction in a system with small wave-packets. Note that to compare simulations with different β values, we fix the peak wave amplitude B_w and check that the average wave intensity $\langle B_w^2 \rangle_{\phi\in[-\infty,+\infty]}$ remains almost the same for different β values, because there is no $\beta \to \infty$ case under consideration and for all simulations the wave field takes ~50% of the ϕ range. Figure 7b1–7b3 show that $\mathcal{M}_2(t)$ for different amplitudes B_w follows the $\sim \bar{D}n$ trend, but there is a difference between fitting coefficients $\bar{D}$ derived for different B_w. This difference is much smaller for smaller β. Figure 7c1–7c3 show $R(B_w)$ for two β values and two magnitudes of wave amplitude modulation. For large β (see panel c1), the effective diffusion rate ratio R increases with B_w: in this case, the nonlinear interactions (trapping and bunching) mix resonant electrons along the resonance curve $m_e c^2\gamma - \omega I_x =$ const much faster than (quasi-linear) diffusion does for the same wave intensity. For small β (see panel c2); this difference in efficiency between nonlinear resonant mixing and diffusive mixing is much less pronounced. The effect of nonlinear interactions becomes even less important for waves with a stronger modulation (see panel c3).

5. Time-Averaged Diffusion Rate $\langle D_{\mathrm{NL}} \rangle$ and $\langle R \rangle = \langle D_{\mathrm{NL}} \rangle / \langle D_{\mathrm{QL}} \rangle$

To finalize the comparison of scattering rates due to diffusion and nonlinear resonances, we perform a massive set of simulations for a wide range of B_w and β parameters and for three typical electron energy and equatorial pitch-angle ranges: ~100 keV, $\alpha_{\mathrm{eq}} \sim 40°$, ~300 keV, $\alpha_{\mathrm{eq}} \sim 50°$, and ~1 MeV, $\alpha_{\mathrm{eq}} \sim 15°$ electrons. For ~100 and ~300 keV simulations, we use the latitudinal profile $B_w(\lambda) = \tanh\left((\lambda/\delta\lambda_1)^2\right)\exp\left(-(\lambda/\delta\lambda_2)^2\right)$ with $\delta\lambda_1 = 2°$ and $\delta\lambda_2 = 20°$ for $\lambda > 0$. This profile mimics the empirical wave intensity distribution with wave growth near the equator and damping at high latitudes obtained from satellite observations (Agapitov et al., 2018). Such latitudinally confined waves cannot resonate with ~1 MeV field-aligned electrons, and for the simulation with ~1 MeV and $\alpha_{\mathrm{eq}} \sim 15°$, we assume ducted wave propagation with $B_w =$ const at all latitudes (Artemyev, Demekhov, et al., 2021; Chen et al., 2022). Figure 8 shows $R(B_w, \beta)$ obtained by fitting the numerical $R(B_w, \beta)$ distributions for these three sets of electron energy/pitch-angles and two magnitudes of wave-packet amplitude modulation. Top panels show results for a realistic, moderate modulation, which potentially allows multiple consecutive trappings in a set of short wave-packets. There are two maxima of R: (a) for long and intense wave packets with $B_w >$ 250pT and $\beta > 100$ which can effectively trap electrons, speeding up electron mixing/diffusion along the resonance curves; (b) for short ($\beta < 15$) and intense ($\beta > 100$) wave packets, in which case electron resonant interactions can include multiple trappings in several successive short packets (Hiraga & Omura, 2020), also speeding up electron mixing/diffusion along the resonance curves. However, spacecraft observations (Zhang, Agapitov, et al., 2020) and numerical simulations of whistler-mode chorus wave generation (Nunn et al., 2021; Zhang et al., 2021) suggest that a significant wave phase decoherence between wave-packets prevents such multiple consecutive trappings and makes electron scattering by these waves more diffusive-like (An et al., 2022;

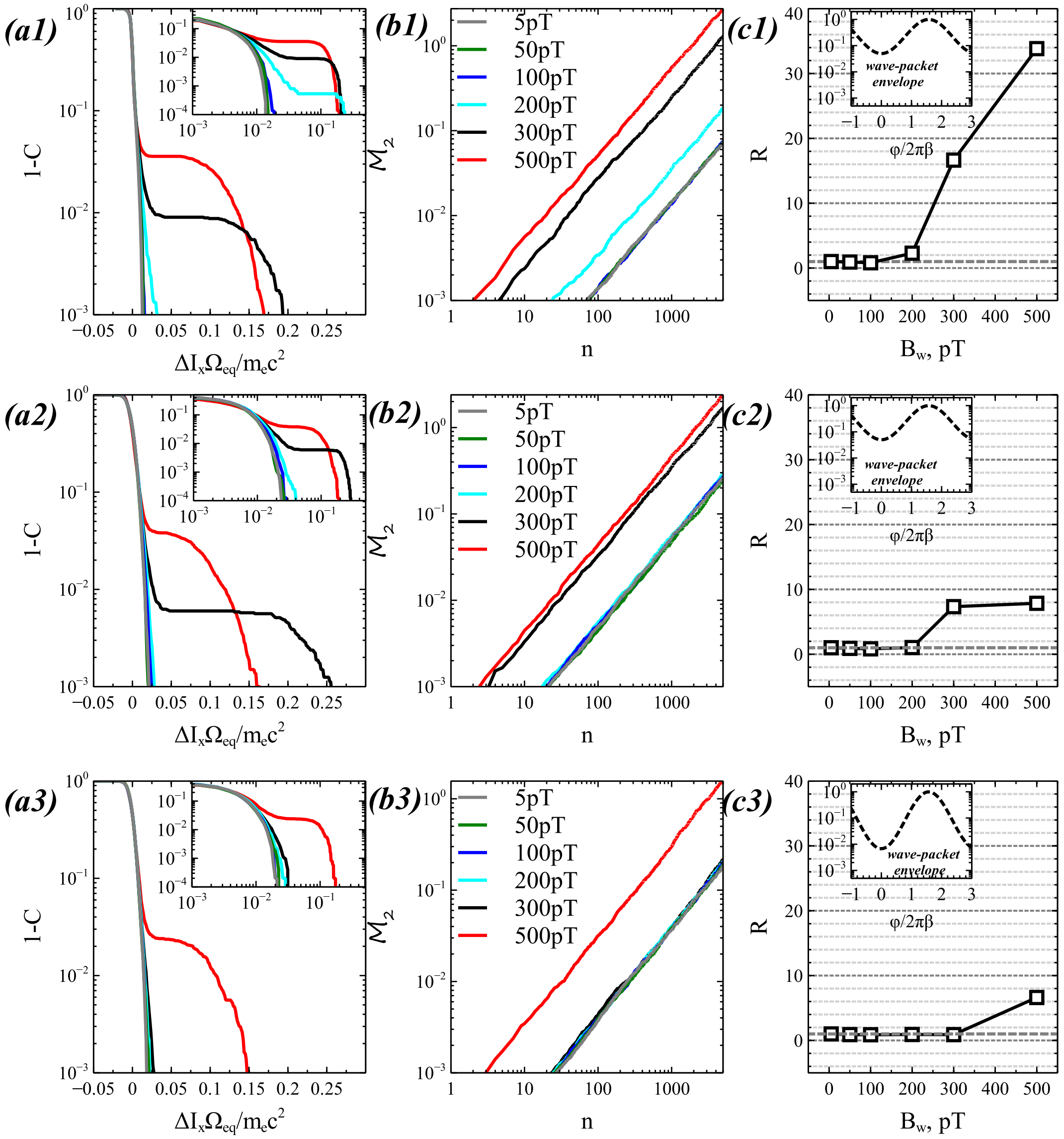

Figure 7. Characteristics of wave-particle resonant interactions for three types of wave-packets: (top row) results for a long wave-packet with a moderate amplitude modulation ($\beta = 300$, and $B_w \propto \exp\left(-3\cos^2(\phi/2\pi\beta)\right)$, with a 5/100 ratio of minimum to maximum wave field amplitudes, see inserted panel in [c1]). (middle row) Results for short wave-packet ($\beta = 3$) with a moderate amplitude modulation. (bottom row) Results for a short wave-packet with strong amplitude modulation ($\beta = 3$ and $B_w \propto \exp\left(-5\cos^2(\phi/2\pi\beta)\right)$, with a 7/1,000 ratio of minimum to maximum wave field amplitude, see inserted panel in [c3]). Panels (a) show the cumulative distributions C of ΔI_x changes for different wave amplitudes (the inserted panels zoom in on the $\Delta I_x > 0$ distributions). Note that in C distributions, ΔI_x is normalized as $\Delta I_x \cdot (B_{w,\max}/B_w)$ to allow comparing $C(\Delta I_x)$ for different wave amplitudes. Panels (b) show $\mathcal{M}_2(n)$ functions obtained with map (6) and $C(\Delta I_x)$ distributions from panels (a). Panels (c) show the ratio $R = \bar{D}(B_w)/\bar{D}(B_{w,\min}) \equiv D_{NL}/D_{QL}$ as a function of wave amplitude. Note that due to the normalization $\Delta I_x \cdot (B_{w,\max}/B_w)$, we expect $R = 1$ for systems in the regime of quasi-linear diffusion. All results are obtained for electrons with [80, 120] keV energies and [30°, 50°] pitch-angles, interacting resonantly with whistler-mode waves at $L = 6$. Wave frequency is $0.35\Omega_{eq}$, plasma frequency is $6\Omega_{eq}$ and constant along magnetic field lines.

Mourenas et al., 2022; Zhang, Agapitov, et al., 2020). Indeed, maxima of R in the small β case are weaker in the bottom panels of Figure 8, where we show simulation results for a strong wave amplitude modulation, due to a reduction of the probability of multiple trappings when the time intervals of high wave amplitude are separated by longer intervals of low amplitude where no nonlinear interaction is possible. The results obtained in the bottom panels of Figure 8 therefore appear more realistic for short $\beta < 15$ wave-packets (An et al., 2022; Gan et al., 2022; Mourenas et al., 2022; Zhang, Agapitov, et al., 2020).

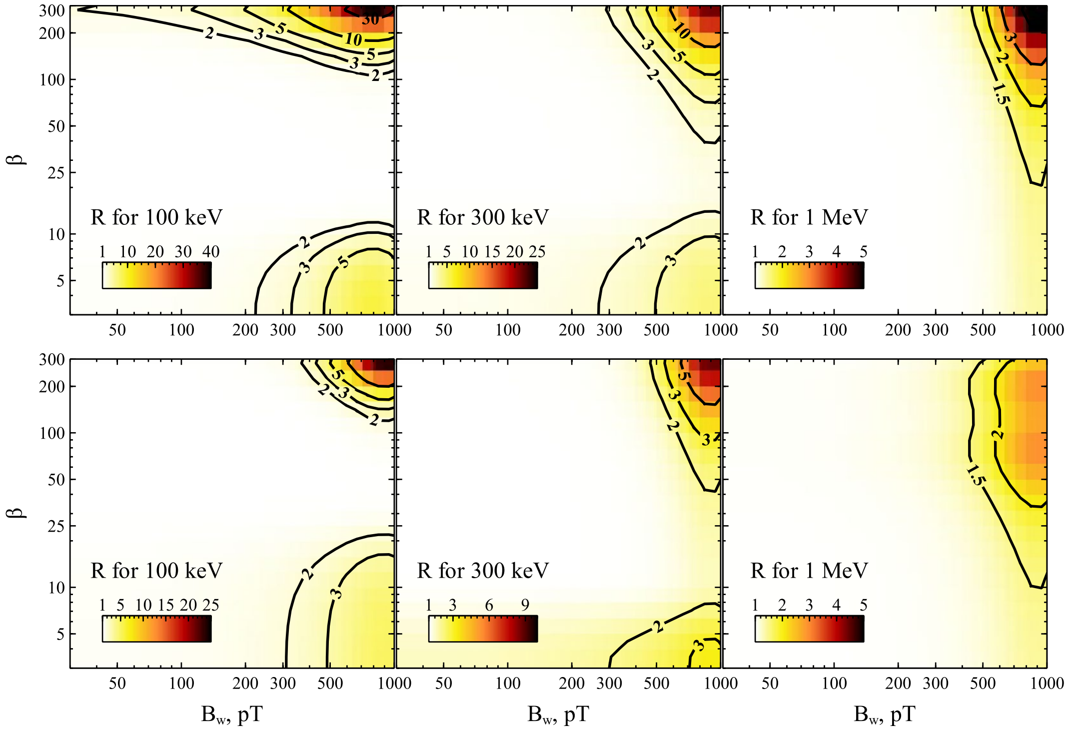

Figure 8. 2D distributions of $R(B_w, \beta)$ ratio for three energy/pitch-angle ranges: (a) ~100 keV, $\alpha_{eq} \sim 40°$, (b) ~300 keV, $\alpha_{eq} \sim 50°$, (c) ~1 MeV, $\alpha_{eq} \sim 15°$. Top panels show results for a moderate wave-packet modulation, and bottom panels show results for a strong modulation that significantly reduces a probability for multiple trapping by successive short wave packets. Background system parameters are: a plasma frequency to electron gyrofrequency ratio at the equator equal to six, a plasma frequency that does not vary along magnetic field lines; a dipolar background geomagnetic field at $L = 6$. Wave frequency is 0.35 times the equatorial electron frequency. The domain with $R = 1$ corresponds to the regime of quasi-linear electron diffusion by whistler-mode waves.

The contribution of nonlinear interactions to electron flux dynamics can be quantified by deviation of R from 1. Thus, to characterize this contribution for the observed distribution of (B_w, β) we must calculate $\langle R\rangle$ averaged over the full wave-packet distribution. Here, we use two different statistics of intense ($B_w > 50$ pT) field-aligned whistler-mode chorus wave packets collected by Zhang et al. (2019) and Zhang, Mourenas, et al. (2020), and we separate each of these two distributions into several subsets corresponding to different levels of geomagnetic activity, $AE < 50$ nT, $AE \in [50, 200]$ nT, $AE \in [200, 500]$ nT, and $AE > 500$ nT. Note that the calculation of D_{NL} requires multiple resonant interactions, and due to the phase trapping effect these interactions spread electrons over a wide energy/pitch-angle domain. Therefore, the present evaluation of R and $\langle R\rangle$ assumes an averaging over this energy/pitch-angle domain, because only such averaging may reduce the fine nonlinear resonant dynamics of individual particles to a diffusive-like dynamics of the particle ensemble, that we describe by $\langle R\rangle\cdot D_{QL}$. Thus, the $\langle R\rangle$ dependence on energy/pitch-angle is nonlocal, and we evaluate here $\langle R\rangle$ for three energy/pitch-angle domains, instead of providing $\langle R\rangle(\gamma, \alpha_{eq})$.

The first empirical distribution of quasi-parallel lower-band chorus wave packets (Zhang et al., 2019) has been derived from 5 years (2012–2017) of Van Allen Probes (Mauk et al., 2013) waveform measurements by the Electric and Magnetic Field Instrument Suite and Integrated Science (EMFISIS) instruments (Kletzing et al., 2013) in the inner magnetosphere, at $L \simeq 4$–6 outside the plasmapause. Using such waveforms, a data set of lower-band chorus wave packets with wave normal angles <25° (calculated using the singular value decomposition method, see Santolík et al., 2003) and peak wave magnetic amplitudes $B_w > 50$ pT has been built, providing a full coverage at geomagnetic latitudes <20° and all local times (Zhang et al., 2019). Starting from the highest peaks of wave amplitude, the boundaries of each packet have been fixed at one half of the packet peak amplitude on both sides. The packet length β was defined as the number of wave periods inside a packet. These selected wave-packets can be either isolated wave-packets or subpackets located inside a longer chorus element. Figure 9 (top) shows the empirical probability distribution $P(B_w, \beta)$ from this first empirical distribution of wave-packets, as a func-

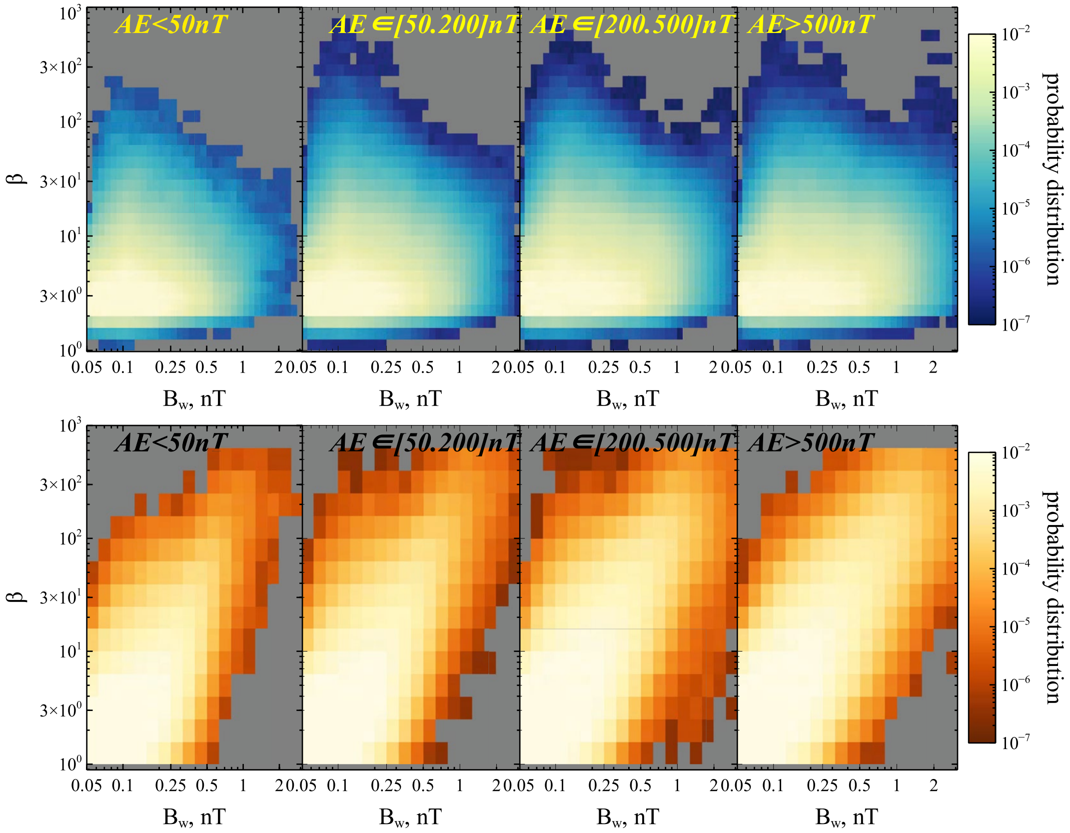

Figure 9. Empirical probability distributions $P(B_w, \beta)$ of intense ($B_w > 50$ pT) whistler-mode chorus wave-packet peak amplitudes B_w and lengths β obtained from 5 to 6 years of Van Allen Probes measurements at $L = 4$–6. (top) Data set provided in Zhang et al. (2019), with wave amplitude equal to $B_w/2$ at wave-packet boundaries. (bottom) Data set provided in Zhang, Mourenas, et al. (2020), with a low wave amplitude ≤50 pT at packet boundaries. Four *AE* ranges are shown.

tion of *AE*. As *AE* increases, the fraction of intense wave-packets increases for all wave-packet sizes β (Zhang et al., 2018) and there are also more long wave-packets, but mainly for moderately intense waves. Waves with very large $B_w > 0.5$–1 nT and $\beta > 100$ are rare even in the highest *AE* range. Therefore, the effect of nonlinear wave-particle interactions should be supported either by the small fraction of long ($\beta > 100$) and moderately intense ($B_w < 500$pT) wave-packets or by the dominant population of relatively short ($\beta < 30$) and intense ($B_w > 250$ pT) wave-packets.

A second empirical distribution of intense wave-packets (Zhang, Mourenas, et al., 2020) has been derived from 6 years of similar Van Allen Probes observations at $L \simeq 4$–6 above the plasmapause. Quasi-parallel lower-band chorus wave-packets have been identified, as before, by a peak of full wave magnetic amplitude $B_w > 50$ pT. However, packet boundaries are now fixed at the nearest wave amplitude minimum below 50 pT or, if this minimum amplitude is below 10 pT, at the time when the wave amplitude diminishes to 10 pT (Zhang, Mourenas, et al., 2020). Such wave-packets are either isolated wave-packets, or subpackets located inside a long rising (or falling) tone chorus element, but also, more rarely, very long wave-packets with not too strong internal modulations. In contrast to the first empirical distribution of wave-packets (Zhang et al., 2019) described above, this second empirical distribution provides packets with a much higher peak amplitude to minimum amplitude ratio. Actual packets with $B_w \sim 300$–1,000 pT, which correspond to the highest nonlinear to quasi-linear effective diffusion rate ratio R in Figure 8 (top), have peak to minimum wave amplitude ratios ~7 to ~40, similar to the moderate amplitude modulation by a factor of 20 used in Figure 7c1, 7c2, and 8 (top). These wave-packets often include weaker but still significant internal amplitude modulations by a factor of ~2 that can terminate particle trapping earlier than based on their full length β (Zhang, Mourenas, et al., 2020), as it can happen also for the ideal sinusoidal modulations used in Figures 7c and 8. It is worth noting that this second empirical distribution of intense wave-packets, shown in Figure 9 (bottom), includes a much larger fraction of very long ($\beta > 100$) and intense

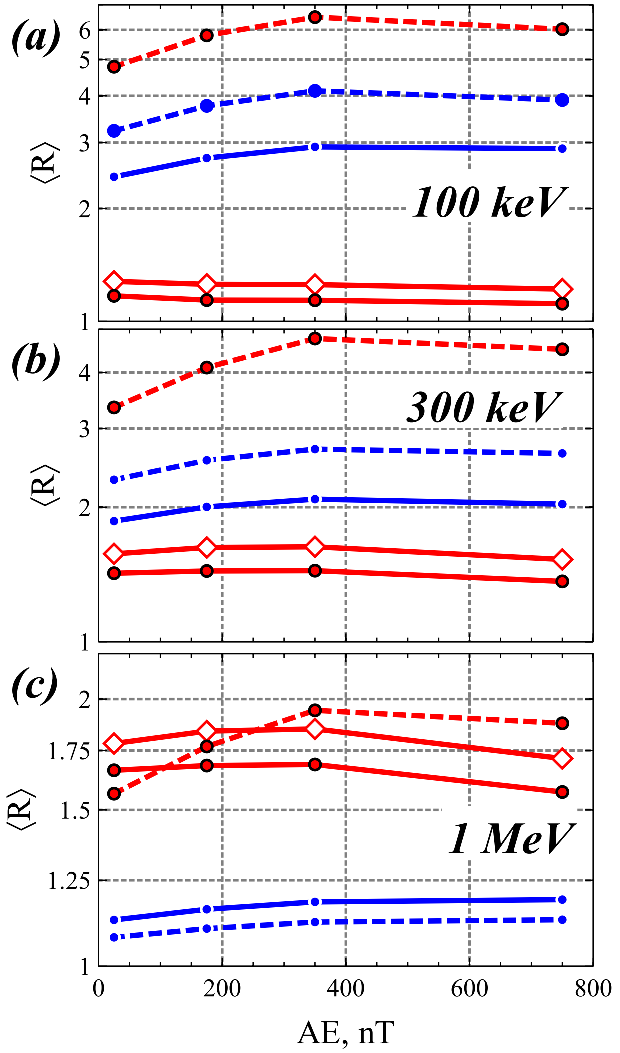

Figure 10. Ratio $\langle R\rangle = \langle \bar{D}(B_w,\beta)\,\bar{\beta}\rangle_{B_w,\beta}/\langle \bar{D}(B_{w,\min},\beta)\,\bar{\beta}\rangle_{\beta} \equiv \langle D_{NL}\rangle/\langle D_{QL}\rangle$ of nonlinear to quasi-linear effective diffusion rates, averaged over two empirical distributions of intense wave-packets (with $B_w > 50$ pT), for two different wave amplitude modulations and three electron energies, as a function of *AE* (with $\bar{\beta} = \beta/\min\beta$). Blue curves show results for the first empirical wave-packet distribution in top panels of Figure 9, using a rescaled probability of occurrence $P(B_w, \beta/3)$. Red curves show results for the second empirical wave-packet distribution in bottom panels of Figure 9, using $P(B_w, \beta)$. Dashed curves show results for a moderate amplitude modulation in simulation packets (as in top panels in Figure 8). Solid red curves show results for the second empirical wave-packet distribution when wave phase decoherence is approximately taken into account by replacing $\bar{D}(B_w,\beta)$ at the numerator and denominator of Equation 7 by $\bar{D}(B_w, L_{coh})\cdot \mathrm{INT}(\beta/L_{coh}) + \bar{D}(B_w,\beta^*)$ for $\beta > L_{\mathrm{coh}}$, where $\beta^* = \beta - L_{\mathrm{coh}}\cdot \mathrm{INT}(\beta/L_{\mathrm{coh}})$ and $L_{\mathrm{coh}} = 50$ (red circles) or $L_{\mathrm{coh}} = 100$ (empty diamonds) wave periods. Solid blue curves show results for the first empirical distribution with a strong amplitude modulation in simulation packets (as in bottom panels in Figure 8). Numbers used for this figure can be found in Table S1 in Supporting Information S1.

(B_w > 250 pT) packets than the first empirical distribution (compare with Figure 9 top), because many of such long and intense packets are split into several shorter packets in the first empirical distribution when their instantaneous amplitude decreases below $B_w/2$. This second empirical distribution of intense chorus wave-packets was found to agree well with results from simulations of nonlinear chorus wave generation performed with various particle codes, in studies where the formation of short and very short packets were respectively ascribed to trapping-induced amplitude modulation and wave superposition (Mourenas et al., 2022; Nunn et al., 2021; Zhang et al., 2021).

Next, we calculate the ratio $\langle R\rangle$ of nonlinear to quasi-linear effective electron diffusion rates averaged over the measured statistical empirical distribution of intense wave-packets, as

$$\langle R\rangle = \frac{\left\langle \bar{D}(B_w,\beta)\cdot\bar{\beta}\right\rangle_{B_w,\beta}}{\left\langle \bar{D}(B_{w,\min},\beta)\cdot\bar{\beta}\right\rangle_{\beta}} \equiv \frac{\langle D_{NL}\rangle}{\langle D_{QL}\rangle}, \tag{7}$$

where averages of $\bar{D}$ are performed using the probability distribution $P(B_w, \beta)$ of the first or second statistics of observed wave-packets, and the factor $\bar{\beta} = \beta/\min(\beta)$ allows to take into account the important fact that the contribution of wave-packets to the time-averaged wave intensity is proportional to their duration β. The ratio $\langle R\rangle$ given by Equation 7, averaged over the full distribution of wave-packets, can be used to rescale classical quasi-linear diffusion rates employed in Fokker-Planck codes, to incorporate the effects of nonlinear resonant interactions.

Figure 10 shows the ratio $\langle R\rangle = \langle D_{\mathrm{NL}}\rangle/\langle D_{\mathrm{QL}}\rangle$ of nonlinear to quasi-linear effective diffusion rates averaged over the two different wave-packet empirical distributions of wave-packets displayed in Figure 9, as a function of *AE* and for three energy/pitch-angle ranges. Typical wave amplitude modulations within packets of the second empirical distribution of (B_w, β) are similar to the moderate modulation used in simulations in Figure 7c1, 7c2, and 8 (top). Therefore, the effective diffusion rates $D(B_w, \beta)$ obtained from simulations with the moderate amplitude modulation has been directly convolved with the probability of occurrence $P(B_w, \beta)$ of the second empirical distribution to obtain $\langle R\rangle$, shown in Figure 10 by dashed red curves. In contrast, all wave-packets of the first empirical distribution are characterized by an amplitude modulation by a factor slightly larger than 2, but much smaller than the factor of 20 used in simulations in Figure 7c1, 7c2, and 8 (top). Employing the same criteria for identifying packets as in the first empirical distribution, the simulation packets would be identified as packets (starting and ending at $B_w/2$) shorter by a factor of 3 than their full length β in simulations. For consistency, the effective diffusion rates $D(B_w, \beta)$ obtained from simulations with a moderate modulation are therefore convolved with the probability of occurrence $P(B_w, \beta/3)$ of these simulation packets in the first empirical distribution. The corresponding estimates of $\langle R\rangle$ are shown in Figure 10 by dashed blue curves.

Figure 10 shows that $\langle R\rangle = \langle D_{\mathrm{NL}}\rangle/\langle D_{\mathrm{QL}}\rangle$ increases with geomagnetic activity from $AE < 50$ nT to $AE \sim 400$ nT, due to an increasing fraction of intense and/or long packets during more disturbed periods (Zhang et al., 2018, 2019). $\langle R\rangle$ averaged over the second empirical distribution of wave-packets (dashed red curves) is significantly higher than $\langle R\rangle$ averaged over the first empirical distribution (dashed blue curves). This is due to a much stronger contribution to $\langle R\rangle$ from long ($\beta > 100$) and intense ($B_w > 250$ pT) packets in the second empirical distribution than in the first one, where such packets are rare. The strongest contribution in the first empirical distribution actually comes from short ($\beta < 10$) and intense ($B_w > 250$ pT) packets that correspond to a lower R than long and intense packets in Figure 8.

How to reconcile the different results obtained for these two different empirical distributions of chorus wave-packets, which have been derived from the same spacecraft measurements simply by using different criteria for the identification of wave-packets? These different results point to the presence of an additional parameter in the system, the presence of wave phase jumps, implicitly taken into account in one empirical distribution but not the other. Strong and random wave frequency and wave phase jumps are known to occur between successive wave-packets over half of a wave period, usually at times when the wave amplitude rapidly decreases to a minimum (usually higher than ∼50 pT), preventing a coherent nonlinear interaction (phase trapping) over consecutive packets (Zhang, Agapitov, et al., 2020; Zhang, Mourenas, et al., 2020) and making it more similar to an interaction with isolated wave-packets (Mourenas et al., 2018; Zhang, Agapitov, et al., 2020). This is consistent for long ($\beta > 50$) packets with what happens in simulations with moderate or strong modulations in Figures 7 and 8, because such long packets are separated in simulations by sufficiently long intervals of low amplitude to prevent consecutive trappings of the same electrons by successive packets during a bounce period. The strong and random wave phase jumps $\Delta\Phi \sim 0.5$–2 rad preventing continuous or successive coherent nonlinear interactions usually correspond to a cluster of 2–4 consecutive wave frequency jumps $\Delta f/f > 0.3$–0.5 (each over a wave half-period) with a simultaneous wave amplitude variation reaching >30–50% of the peak amplitude (Zhang, Agapitov, et al., 2020).

However, Zhang, Mourenas, et al. (2020) have shown that such strong frequency jumps $\Delta f/f > 0.5$ also occur on average over ∼3% of the wave half-periods in the heart of long ($\beta > 50$) wave-packets, with a statistical occurrence rate remarkably independent of packet length β. Such strong frequency jumps typically occur in clusters of ∼3 jumps in as many consecutive wave half-periods, each cluster corresponding to one phase jump (Zhang, Agapitov, et al., 2020; Zhang, Mourenas, et al., 2020). This suggests a maximum wave phase coherence length of $L_{\mathrm{coh}} \simeq 50$–100 wave periods for long packets with $\beta > 50$, in agreement with previous estimates (Agapitov et al., 2017). This is consistent with the near absence of long ($\beta > 50$–100) and intense ($B_w > 0.25$ nT) packets in the first empirical distribution in Figure 9 (top), which implies that nearly all such long packets in the second statistics actually contain strong wave amplitude (by at least a factor of 2) and wave phase jumps that likely limit coherent nonlinear interaction to $L_{\mathrm{coh}} < 50$–100 wave periods. Such wave phase decoherence within long packets is already roughly taken into account in the first empirical distribution in Figure 9 (top), where long packets have already been split into several shorter packets when their amplitude decreases below half of their peak amplitude (Zhang, Mourenas, et al., 2020). However, it is not taken into account in the second empirical distribution, leading to an overestimation of nonlinear effects and $\langle R\rangle$.

To include such wave phase decoherence effects in the second empirical distribution of wave-packets, we assume to first order that all long packets with $\beta > L_{\mathrm{coh}} \simeq 50$–100 correspond to a coherent nonlinear interaction limited to independent sub-intervals of $\beta = L_{\mathrm{coh}}$ (or less) wave periods. This is done by replacing $\bar{D}(B_w, \beta)$ at the numerator and denominator of Equation 7, by $\bar{D}(B_w, L_{coh}) \cdot \mathrm{INT}(\beta/L_{coh}) + \bar{D}(B_w, \beta^*)$ for $\beta > L_{\mathrm{coh}}$, keeping the same probability distribution $P(B_w, \beta)$ as before, with INT(x) the floor (or integer) function and $\beta^* = \beta - L_{\mathrm{coh}} \cdot \mathrm{INT}(\beta/L_{\mathrm{coh}})$. The resulting refined estimates of $\langle R\rangle$ for the second empirical statistics are shown in Figure 10 by solid red curves, with red circles for $L_{\mathrm{coh}} = 50$ and with white diamonds for $L_{\mathrm{coh}} = 100$. One can see that $\langle R\rangle$ is strongly reduced by phase decoherence (compare dashed red and solid red curves). But the difference between results for the first and second empirical distributions (dashed blue and solid red curves, respectively) remains similar, or even increased at 100 keV where $\langle R\rangle$ for the second empirical distribution is now smaller than for the first one.

Although our approximate inclusion of wave phase decoherence effects in the evaluation of $\langle R\rangle$ for the second statistics may lead to some underestimation of $\langle R\rangle$, one additional effect must be taken into account in the case of the first empirical distribution of packets. For short and intense packets with $\beta < 10$–20, which strongly contribute to $\langle R\rangle$ for the first statistics but almost do not contribute for the second empirical distribution, the simulations in Figure 8 (top) sometimes contain consecutive trappings (Hiraga & Omura, 2020) that are absent in most cases for real short packets, because the latter are usually separated by strong random wave phase jumps (Zhang, Agapitov, et al., 2020). This inclusion of consecutive trappings implies a probable overestimation of $\langle R\rangle$ calculated for the first empirical distribution using simulation packets with moderate amplitude modulation (dashed blue curves). To suppress this overestimation, $\langle R\rangle$ is now calculated for the first empirical distribution based on simulations with packets possessing a strong modulation, as in Figure 7c3 and 8 (bottom). In such simulations, the occurrence of multiple trappings in consecutive short packets is indeed sensibly reduced as compared with simulations using packets with a moderate modulation. The resulting more realistic estimate of $\langle R\rangle$ for the first empirical distribution is shown by solid blue curves in Figure 10. Our two final estimates of $\langle R\rangle$ based on the first and second empirical distributions of wave-packets (solid blue and solid red curves, respectively) are relatively close to each other, especially at 300 keV and 1 MeV, demonstrating a rough consistency. The remaining differences illustrate the remaining uncertainties in our approximate models of chorus wave-packet amplitude modulations and wave phase decoherence.

For 100–300 keV electrons with $\alpha_{\mathrm{eq}} \sim 40°$–$50°$, our estimates of $\langle R\rangle$ (solid blue and red curves in Figure 10) are comprised between $\sim$1.2–1.5 and $\sim$2–3, with only a slight increase from low ($AE < 50$ nT) to high ($AE = 350$ nT) geomagnetic activity. Therefore, such electrons can be accelerated $\sim$1.5–3 times faster when nonlinear resonant interactions with intense wave-packets are taken into account, as compared with a purely diffusive (quasi-linear) acceleration. This faster electron acceleration can be present during disturbed periods (e.g., during geomagnetic storms or prolonged periods of substorms, see Li et al., 2014; Thorne et al., 2013) characterized by whistler-mode waves more often reaching time-averaged amplitudes higher than 50 pT (Zhang et al., 2018), because the corresponding wave-packets reach significantly higher peak amplitudes, often sufficient to enter the nonlinear regime of wave-particle interaction (e.g., see Artemyev, Agapitov, et al., 2016; Cully et al., 2011). The moderate increase of $\langle R\rangle$ with AE is probably due to a dominant contribution from moderately long ($\beta < 30$–100) and not too intense ($B_w < 0.8$ nT) wave-packets, whose distribution does not change significantly with AE in Figure 9. The very slight decrease of $\langle R\rangle$ for $AE > 500$ nT apparently comes from a slight reduction of β for this population of wave-packets, but this variation may not be real because there are less data and larger uncertainties in distribution parameters during such highly disturbed periods.

For 1 MeV electrons with $\alpha_{\mathrm{eq}} \sim 15°$, cyclotron resonance can be reached only at high magnetic latitudes, where the background geomagnetic field gradient is sufficiently strong to prevent nonlinear resonant interaction for moderately intense waves, whereas the occurrence rate of intense ($B_w > 0.5$ nT) waves (see Figure 8, right panel) is not sufficiently high (see Figure 9) to strongly increase the average $\langle R\rangle$. As a result, $\langle R\rangle$ remains in the range $\sim$1.2–1.9 from low to high AE for such electrons. The corresponding increase of the loss rate of 1-MeV electrons is similar to the increase of the acceleration rate of 100–300 keV electrons. However, it is worth remembering that ducted propagation of the waves up to high latitudes has been assumed to calculate $\langle R\rangle$ for 1 MeV electrons (Artemyev, Demekhov, et al., 2021; Chen et al., 2022; Zhang, Angelopoulos, et al., 2022). In the opposite but more frequent case of unducted wave propagation, the waves would rapidly become more oblique and, in general, would be heavily damped before reaching the latitude of resonance with 1 MeV electrons (Chen et al., 2021). Consequently, the time intervals with intense, ducted chorus waves should be characterized by a faster increase of 1-MeV electron flux and by stronger precipitations of 1-MeV electrons (Chen et al., 2022; Miyoshi et al., 2020; Zhang, Angelopoulos, et al., 2022) than in calculations assuming a purely quasi-linear electron diffusion (Mourenas, Artemyev, Agapitov, & Krasnoselskikh, 2014; Mourenas, Artemyev, Agapitov, Krasnoselskikh, & Li, 2014), but it may not be the case during the more frequent periods with unducted wave propagation.

However, it is worth emphasizing that $\langle R\rangle$ has been evaluated above (in Figure 10) solely based on empirical distributions of intense chorus wave-packets with amplitudes $B_w > 50$ pT. Such intense wave-packets can be observed during both periods of weak and strong geomagnetic activity, with similar (B_w, β) distributions of packets contributing the most to $\langle R\rangle$. However, such intense wave-packets are mainly observed during disturbed periods, like storms and substorms (Zhang et al., 2018), and less frequently during quiet periods. Figure 11a shows the fraction F_{iwp} of total chorus wave power contained in such intense wave-packets (with $B_w > 50$ pT), obtained from 9 months of lower-band chorus waves measurements by the Van Allen Probes in March-November 2017, demonstrating that this fraction F_{iwp} indeed increases from $\sim$30% to $\sim$45% as AE increases from 50 to 1,000 nT. This full distribution of wave power can be used to estimate the full statistical ratio $\langle R\rangle_{\mathrm{stat}} \equiv \langle D_{\mathrm{NL}}\rangle / \langle D_{\mathrm{QL}}\rangle$ of effective (nonlinear and quasi-linear) to quasi-linear diffusion rates of electrons in the outer radiation belt, averaged over all (weak and intense) chorus waves observed during periods within a given AE range, by replacing $\langle \bar{D}(B_w,\beta)\cdot\bar{\beta}\rangle_{B_w,\beta}$ by $F_{iwp} \times \langle \bar{D}(B_w,\beta)\cdot\bar{\beta}\rangle_{B_w,\beta} + (1-F_{iwp}) \times \langle \bar{D}(B_{w,\mathrm{min}},\beta)\cdot\bar{\beta}\rangle\rangle_{\beta}$ in Equation 7.

Figures 11b–11d show the corresponding full statistical ratio $\langle R\rangle_{\mathrm{stat}}$ averaged over all (weak and intense) waves for 100 and 300 keV electrons with $\alpha_{\mathrm{eq}} \sim 40°$–$50°$ and for 1 MeV electrons near the loss-cone, in the same format as in Figure 10 for $\langle R\rangle$ averaged only over intense wave-packets. All full statistical ratios $\langle R\rangle_{\mathrm{stat}}$ in Figure 11 are sensibly smaller than the corresponding intense packet ratios $\langle R\rangle$ in Figure 10, because intense wave-packets susceptible to produce nonlinear effects contain only F_{iwp}<50% of the total wave power. As in Figure 10, solid blue and

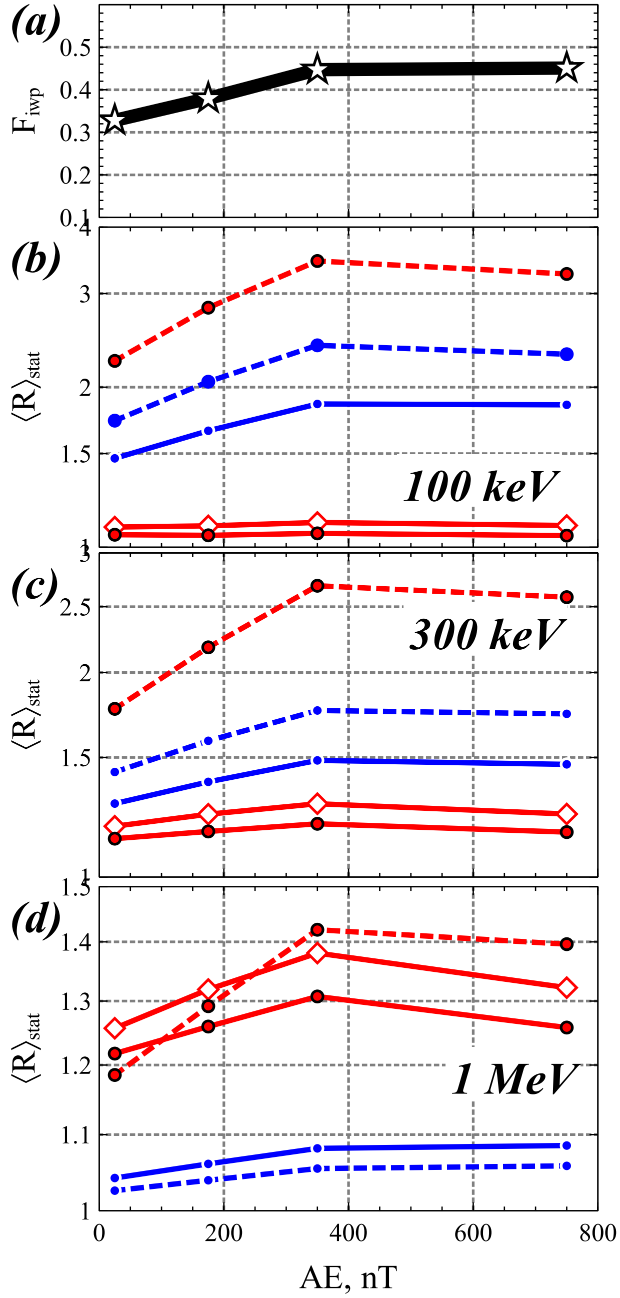

Figure 11. (a) Fraction F_{iwp} of the total lower-band chorus wave power contained by intense wave-packets (with $B_w > 50$ pT) as a function of AE, based on 9 months of Van Allen Probe measurements. (b–d) Full statistical ratio $\langle R\rangle_{\text{stat}} \equiv \langle D_{\text{NL}}\rangle/\langle D_{\text{QL}}\rangle$ of nonlinear to quasi-linear effective diffusion rates, averaged over the full distribution of chorus waves (including both intense packets and weak waves), for three electron energies and for two empirical distributions of intense wave-packets, as a function of AE. All curves show the same results as in Figure 10, but $\langle \bar{D}(B_w,\beta)\cdot\bar{\beta}\rangle_{B_w,\beta}$ has been replaced by $F_{iwp}\times\langle \bar{D}(B_w,\beta)\cdot\bar{\beta}\rangle_{B_w,\beta} + \left(1 - F_{iwp}\right)\times\langle \bar{D}(B_{w,\min},\beta)\cdot\bar{\beta}\rangle_{\beta}$ in Equation 7. Numbers used for this figure can be found in Table S2 in Supporting Information S1.

red curves show the most realistic and consistent estimates of $\langle R\rangle_{\text{stat}}$, obtained using the two different empirical distributions of intense wave-packets from Figure 9. Solid blue curves show results based on the first empirical distribution of intense packets, with a strong amplitude modulation in simulation packets, using a rescaled probability of occurrence $P(B_w, \beta/3)$. Solid red curves show results based on the second empirical distribution of intense packets in Figure 9, using $P(B_w, \beta)$, with wave phase decoherence taken into account by replacing $\bar{D}(B_w,\beta)$ by $\bar{D}(B_w, L_{coh})\cdot \text{INT}(\beta/L_{coh}) + \bar{D}(B_w,\beta^*)$ for $\beta > L_{\text{coh}}$, where $\beta^* = \beta - L_{\text{coh}}\cdot \text{INT}(\beta/L_{\text{coh}})$ and $L_{\text{coh}} = 50$ (red circles) or $L_{\text{coh}} = 100$ (empty diamonds) wave periods. One can see that the full statistical $\langle R\rangle_{\text{stat}}$, now calculated over both periods of intense waves and periods of weak waves, increases with AE in all cases. As AE increases from 50 nT to 400–800 nT, the statistical ratio $\langle R\rangle_{\text{stat}}$ increases from 1.07–1.5 to 1.12–2.0 at 100 keV, from 1.2–1.3 to 1.25–1.5 at 300 keV, and from 1.05–1.25 to 1.1–1.35 at 1 MeV.

6. Conclusions

In this paper, we have proposed an approach for the derivation of a rescaling factor $R = D_{\text{NL}}/D_{\text{QL}}$ of the classical quasi-linear diffusion rate D_{QL} of electrons by whistler-mode waves, allowing in principle to incorporate long-term effects of nonlinear resonant interactions into Fokker-Planck radiation belt codes in a simple and practicable way. We considered a generalized, effective nonlinear diffusion rate D_{NL} that would result in the same time-scale of electron distribution relaxation along resonance curves as the corresponding time-scale of evolution due to nonlinear interactions. We first noted that the ratio $R = D_{\text{NL}}/D_{\text{QL}}$ depends on two main system parameters: wave intensity, B_w^2, wave packet length/duration, β. We proposed an approach for evaluating D_{NL} for fixed wave characteristics.

Next, we provided the average rescaling factor $\langle R\rangle = \langle D_{\text{NL}}\rangle/\langle D_{\text{QL}}\rangle$ of quasi-linear diffusion rates D_{QL}, averaged over empirical distributions of intense whistler-mode chorus wave-packet characteristics $\left(B_w^2, \beta\right)$, derived from years of Van Allen Probes measurements at $L = 4$–6 of intense packets with $B_w > 50$ nT. This rescaling factor has been evaluated for three energy/pitch-angle ranges of key importance in the outer radiation belt: ~1 MeV electrons with small pitch-angles and ~100–300 keV electrons with medium/large pitch-angles. We found that $\langle R\rangle$ increases only weakly with geomagnetic activity (AE) and that nonlinear effects can speed up 0.1–1 MeV electron diffusive acceleration by a factor of ×2–3, while only slightly increasing the loss rate of 1-MeV electrons by a factor of ×1.5 (in the latter case, only for ducted wave propagation). The finite differences between our two different estimates of $\langle R\rangle$, based on two different empirical distributions of the same chorus wave-packets obtained using different wave-packet selection criteria, suggest that the effects of wave phase coherence on nonlinear interactions deserve further study. In particular, a further analysis of statistical properties of wave phase jumps inside wave-packets would be useful, as well as a more precise analysis of their effects in simulations.

But the ratio $\langle R\rangle(AE)$ discussed above has been evaluated based solely on empirical distributions of intense chorus wave-packets, with amplitudes $B_w > 50$ pT. However, such intense wave-packets are observed more frequently during disturbed periods, like geomagnetic storms and substorms, than during quiet times (Zhang et al., 2018). Therefore, a second, more realistic statistical ratio $\langle R\rangle_{\text{stat}}(AE) = \langle D_{\text{NL}}\rangle/\langle D_{\text{QL}}\rangle$ has been calculated by averaging nonlinear and quasi-linear diffusion rates over all chorus waves, intense ($B_w > 50$ pT) and weak ($B_w < 50$ pT), observed during periods within a given AE range. This full statistical ratio $\langle R\rangle_{\text{stat}}$ does increase with geomagnetic activity, varying from $\langle R\rangle_{\text{stat}} \sim 1.0$–$1.2$ during quiet periods to $\langle R\rangle_{\text{stat}} \sim 1.35$–$2.0$ when $AE \sim 400$–800 nT, corresponding to strong substorms with important low-energy electron injections leading to the generation of intense wave-packets with $B_w > 50$ pT (Meredith et al., 2003; Li et al., 2009, 2011; Zhang et al., 2018).

The obtained statistical rescaling factor $\langle R\rangle_{\text{stat}}$ of quasi-linear diffusion rates accounts for the contribution of nonlinear resonant interactions in long-term electron flux dynamics. Note that $\langle R\rangle_{\text{stat}}$ can be significantly different from 1 only in the presence of sufficiently intense wave-packets, above the threshold for nonlinear resonant interaction. But it is worth emphasizing that chorus wave-packets usually reach peak amplitudes much larger than the (3-s to hourly) root-mean-squared time-averaged amplitudes of chorus waves, and that the threshold amplitude for nonlinear interaction can typically vary between 100 and 500 pT at $L = 4$–6, depending on electron energy and pitch-angle, on the background geomagnetic field inhomogeneity, and on the latitudinal wave power profile (Albert et al., 2013; Artemyev, Agapitov, et al., 2016). Accordingly, this rescaling factor $\langle R\rangle_{\text{stat}}$ should be carefully calculated in each parameter domain wherein nonlinear interactions are potentially available.

Increasing quasi-linear electron diffusion rates by factors $\langle R\rangle_{\text{stat}} \sim 1.5$–$2.0$ over long intervals of disturbances may have a profound impact on the long-term dynamics of ~0.1–5 MeV electron fluxes, because electron diffusive acceleration is a gradual process such that a small fraction of the abundant low-energy electrons injected from the plasma sheet can ultimately be transported to much higher energy, where the electron flux is initially very small. As a result, even a limited increase in diffusion rate due to nonlinear interactions can potentially lead to a significant increase of >1 MeV electron fluxes over hours to days. Including such nonlinear effects into radiation belt codes could therefore probably help to better reproduce and forecast the dynamics of relativistic electron fluxes over the long run.

During shorter periods (less than a few hours), the nonlinear increase of electron diffusion rates can occasionally reach higher values than the full statistical ratio $\langle R\rangle_{\text{stat}}$, when intense wave-packets are more frequent than in month-averaged statistics. In this case, the factor of increase of quasi-linear diffusion rates should be closer to $\langle R\rangle$ averaged only over intense wave-packets, potentially reaching higher values $\langle R\rangle \sim 2$–3. This could explain some of the apparent step-like increases of relativistic electron flux observed within intervals of tens of minutes to a few hours by the Van Allen Probes during storms or substorms (Foster et al., 2017; Murphy et al., 2018; Thorne et al., 2013).

Finally, it is worth noting that the present approach of rescaling quasi-linear diffusion coefficients to take into account nonlinear effects requires electron mixing in the energy/pitch-angle space over a sufficient time (about 1 hour or more) to make the electron distribution evolution more diffusive after averaging over a large number of nonlinear resonant interactions. It definitely does not work for short-time effects (like microbursts), but should work over time scales of hours, like during a typical storm. Such a description should provide the change of the variation rate of the electron distribution due to nonlinear effects, but it cannot reproduce any fine transient changes to this distribution.

Data Availability Statement

The authors acknowledge the Van Allen Probes EMFISIS data obtained from https://emfisis.physics.uiowa.edu/data/index. Data access and processing was done using SPEDAS V4.1 Angelopoulos et al. (2019) available at https://spedas.org/. Main research results, $\langle R\rangle$ profiles shown in Figures 10 and 11 are provided in tables in Supporting Information S1.

Acknowledgments
A.V.A. and X.-J.Z. acknowledge support by NASA awards 80NSSC21K0729 and 80NSSC22K0522, D.V. acknowledges support by NASA award 80NSSC19K0266, and A.V.A. acknowledge support by NSF grants NSF-2026375.

References

Agapitov, O. V., Artemyev, A., Krasnoselskikh, V., Khotyaintsev, Y. V., Mourenas, D., Breuillard, H., et al. (2013). Statistics of whistler mode waves in the outer radiation belt: Cluster STAFF-SA measurements. *Journal of Geophysical Research*, *118*(6), 3407–3420. https://doi.org/10.1002/jgra.50312

Agapitov, O. V., Artemyev, A., Mourenas, D., Krasnoselskikh, V., Bonnell, J., Le Contel, O., et al. (2014). The quasi-electrostatic mode of chorus waves and electron nonlinear acceleration. *Journal of Geophysical Research*, *119*(3), 1606–1626. https://doi.org/10.1002/2013JA019223

Agapitov, O. V., Artemyev, A. V., Mourenas, D., Mozer, F. S., & Krasnoselskikh, V. (2015). Nonlinear local parallel acceleration of electrons through Landau trapping by oblique whistler mode waves in the outer radiation belt. *Geophysical Research Letters*, *42*(23), 10. https://doi.org/10.1002/2015GL066887

Agapitov, O. V., Blum, L. W., Mozer, F. S., Bonnell, J. W., & Wygant, J. (2017). Chorus whistler wave source scales as determined from multipoint Van Allen Probe measurements. *Geophysical Research Letters*, *44*(6), 2634–2642. https://doi.org/10.1002/2017GL072701

Agapitov, O. V., Mourenas, D., Artemyev, A. V., Mozer, F. S., Hospodarsky, G., Bonnell, J., & Krasnoselskikh, V. (2018). Synthetic empirical chorus wave model from combined Van Allen Probes and Cluster statistics. *Journal of Geophysical Research (Space Physics)*, *123*(1), 297–314. https://doi.org/10.1002/2017JA024843

Albert, J. M. (2000). Gyroresonant interactions of radiation belt particles with a monochromatic electromagnetic wave. *Journal of Geophysical Research*, *105*(A9), 21191–21209. https://doi.org/10.1029/2000JA000008

Albert, J. M. (2001). Comparison of pitch angle diffusion by turbulent and monochromatic whistler waves. *Journal of Geophysical Research*, *106*(A5), 8477–8482. https://doi.org/10.1029/2000JA000304

Albert, J. M. (2010). Diffusion by one wave and by many waves. *Journal of Geophysical Research*, *115*(A3), A04219. https://doi.org/10.1029/2009JA014732

Albert, J. M., & Bortnik, J. (2009). Nonlinear interaction of radiation belt electrons with electromagnetic ion cyclotron waves. *Geophysical Research Letters*, *36*(12), 12110. https://doi.org/10.1029/2009GL038904

Albert, J. M., Tao, X., & Bortnik, J. (2013). Aspects of nonlinear wave-particle interactions. In D. Summers, I. U. Mann, D. N. Baker, & M. Schulz (Eds.), *Dynamics of the earth's radiation belts and inner magnetosphere*. American Geophysical Union. https://doi.org/10.1029/2012GM001324

Allanson, O., Thomas, E., Watt, C. E. J., & Neukirch, T. (2022). Weak turbulence and quasilinear diffusion for relativistic wave-particle interactions via a Markov approach. *Frontiers in Physics*, *8*, 805699. https://doi.org/10.3389/fspas.2021.805699

Allanson, O., Watt, C. E. J., Allison, H. J., & Ratcliffe, H. (2021). Electron diffusion and advection during nonlinear interactions with whistler mode waves. *Journal of Geophysical Research (Space Physics)*, *126*(5), e28793. https://doi.org/10.1029/2020JA028793

Allanson, O., Watt, C. E. J., Ratcliffe, H., Allison, H. J., Meredith, N. P., Bentley, S. N., et al. (2020). Particle-in-Cell experiments examine electron diffusion by whistler-mode waves: 2. Quasi-linear and nonlinear dynamics. *Journal of Geophysical Research (Space Physics)*, *125*(7), e27949. https://doi.org/10.1029/2020JA027949

Allison, H. J., & Shprits, Y. Y. (2020). Local heating of radiation belt electrons to ultra-relativistic energies. *Nature Communications*, *11*(1), 4533. https://doi.org/10.1038/s41467-020-18053-z

An, Z., Wu, Y., & Tao, X. (2022). Electron dynamics in a chorus wave field generated from particle-in-cell simulations. *Geophysical Research Letters*, *49*(3), e97778. https://doi.org/10.1029/2022GL097778

Andronov, A. A., & Trakhtengerts, V. Y. (1964). Kinetic instability of the Earth's outer radiation belt. *Geomagnetism and Aeronomy*, *4*, 233–242.

Angelopoulos, V., Cruce, P., Drozdov, A., Grimes, E. W., Hatzigeorgiu, N., King, D. A., et al. (2019). The space Physics environment data analysis system (SPEDAS). *Space Science Reviews*, *215*(1), 9. https://doi.org/10.1007/s11214-018-0576-4

Artemyev, A. V., Agapitov, O., Mourenas, D., Krasnoselskikh, V., Shastun, V., & Mozer, F. (2016). Oblique whistler-mode waves in the Earth's inner magnetosphere: Energy distribution, origins, and role in radiation belt dynamics. *Space Science Reviews*, *200*(1–4), 261–355. https://doi.org/10.1007/s11214-016-0252-5

Artemyev, A. V., Demekhov, A. G., Zhang, X. J., Angelopoulos, V., Mourenas, D., Fedorenko, Y. V., et al. (2021). Role of ducting in relativistic electron loss by whistler-mode wave scattering. *Journal of Geophysical Research (Space Physics)*, *126*(11), e29851. https://doi.org/10.1029/2021JA029851

Artemyev, A. V., Krasnoselskikh, V., Agapitov, O., Mourenas, D., & Rolland, G. (2012). Non-diffusive resonant acceleration of electrons in the radiation belts. *Physics of Plasmas*, *19*(12), 122901. https://doi.org/10.1063/1.4769726

Artemyev, A. V., Neishtadt, A. I., & Angelopoulos, V. (2022). On the role of whistler-mode waves in electron interaction with dipolarizing flux bundles. *Journal of Geophysical Research: Space Physics*, *127*(4), e2022JA030265. https://doi.org/10.1029/2022JA030265

Artemyev, A. V., Neishtadt, A. I., Vainchtein, D. L., Vasiliev, A. A., Vasko, I. Y., & Zelenyi, L. M. (2018). Trapping (capture) into resonance and scattering on resonance: Summary of results for space plasma systems. *Communications in Nonlinear Science and Numerical Simulation*, *65*, 111–160. https://doi.org/10.1016/j.cnsns.2018.05.004

Artemyev, A. V., Neishtadt, A. I., & Vasiliev, A. A. (2020a). A map for systems with resonant trappings and scatterings. *Regular & Chaotic Dynamics*, *25*(1), 2–10. https://doi.org/10.1134/S1560354720010025

Artemyev, A. V., Neishtadt, A. I., & Vasiliev, A. A. (2020b). Mapping for nonlinear electron interaction with whistler-mode waves. *Physics of Plasmas*, *27*(4), 042902. https://doi.org/10.1063/1.5144477

Artemyev, A. V., Neishtadt, A. I., Vasiliev, A. A., & Mourenas, D. (2016). Kinetic equation for nonlinear resonant wave-particle interaction. *Physics of Plasmas*, *23*(9), 090701. https://doi.org/10.1063/1.4962526

Artemyev, A. V., Neishtadt, A. I., Vasiliev, A. A., & Mourenas, D. (2018). Long-term evolution of electron distribution function due to nonlinear resonant interaction with whistler mode waves. *Journal of Plasma Physics*, *84*(2), 905840206. https://doi.org/10.1017/S0022377818000260

Artemyev, A. V., Neishtadt, A. I., Vasiliev, A. A., & Mourenas, D. (2021). Transitional regime of electron resonant interaction with whistler-mode waves in inhomogeneous space plasma. *Physical Review E*, *104*(5), 055203. https://doi.org/10.1103/PhysRevE.104.055203

Artemyev, A. V., Neishtadt, A. I., Vasiliev, A. A., Zhang, X.-J., Mourenas, D., & Vainchtein, D. (2021). Long-term dynamics driven by resonant wave-particle interactions: From Hamiltonian resonance theory to phase space mapping. *Journal of Plasma Physics*, *87*(2), 835870201. https://doi.org/10.1017/S0022377821000246

Artemyev, A. V., Vasiliev, A. A., Mourenas, D., Agapitov, O. V., & Krasnoselskikh, V. V. (2014). Electron scattering and nonlinear trapping by oblique whistler waves: The critical wave intensity for nonlinear effects. *Physics of Plasmas*, *21*(10), 102903. https://doi.org/10.1063/1.4897945

Artemyev, A. V., Vasiliev, A. A., Mourenas, D., Neishtadt, A. I., Agapitov, O. V., & Krasnoselskikh, V. (2015). Probability of relativistic electron trapping by parallel and oblique whistler-mode waves in Earth's radiation belts. *Physics of Plasmas*, *22*(11), 112903. https://doi.org/10.1063/1.4935842

Artemyev, A. V., Vasiliev, A. A., & Neishtadt, A. I. (2019). Charged particle nonlinear resonance with localized electrostatic wave-packets. *Communications in Nonlinear Science and Numerical Simulation*, *72*, 392–406. https://doi.org/10.1016/j.cnsns.2019.01.011

Benkadda, S., Sen, A., & Shklyar, D. R. (1996). Chaotic dynamics of charged particles in the field of two monochromatic waves in a magnetized plasma. *Chaos*, *6*(3), 451–460. https://doi.org/10.1063/1.166187

Bortnik, J., Thorne, R. M., & Inan, U. S. (2008). Nonlinear interaction of energetic electrons with large amplitude chorus. *Geophysical Research Letters*, *35*(21), 21102. https://doi.org/10.1029/2008GL035500

Breneman, A. W., Crew, A., Sample, J., Klumpar, D., Johnson, A., Agapitov, O., et al. (2017). Observations directly linking relativistic electron microbursts to whistler mode chorus: Van Allen Probes and FIREBIRD II. *Geophysical Research Letters*, *44*(22), 11265–11272. https://doi.org/10.1002/2017GL075001

Cary, J. R., Escande, D. F., & Tennyson, J. L. (1986). Adiabatic-invariant change due to separatrix crossing. *Physical Review A*, *34*(5), 4256–4275. https://doi.org/10.1103/physreva.34.4256

Cattell, C., Wygant, J. R., Goetz, K., Kersten, K., Kellogg, P. J., von Rosenvinge, T., et al. (2008). Discovery of very large amplitude whistler-mode waves in Earth's radiation belts. *Geophysical Research Letters*, *35*(1), 1105. https://doi.org/10.1029/2007GL032009

Chen, L., Zhang, X.-J., Artemyev, A., Angelopoulos, V., Tsai, E., Wilkins, C., & Horne, R. B. (2022). Ducted chorus waves cause sub-relativistic and relativistic electron microbursts. *Geophysical Research Letters*, *49*(5), e97559. https://doi.org/10.1029/2021GL097559

Chen, L., Zhang, X.-J., Artemyev, A., Zheng, L., Xia, Z., Breneman, A. W., & Horne, R. B. (2021). Electron microbursts induced by nonducted chorus waves. *Frontiers in Astronomy and Space Sciences*, *8*, 163. https://doi.org/10.3389/fspas.2021.745927

Chen, L., Zhu, H., & Zhang, X. (2019). Wavenumber analysis of EMIC waves. *Geophysical Research Letters*, *46*(11), 5689–5697. https://doi.org/10.1029/2019GL082686

Chirikov, B. V. (1979). A universal instability of many-dimensional oscillator systems. *Physics Reports*, *52*(5), 263–379. https://doi.org/10.1016/0370-1573(79)90023-1

Cully, C. M., Angelopoulos, V., Auster, U., Bonnell, J., & Le Contel, O. (2011). Observational evidence of the generation mechanism for rising-tone chorus. *Geophysical Research Letters*, *38*(1), 1106. https://doi.org/10.1029/2010GL045793

Cully, C. M., Bonnell, J. W., & Ergun, R. E. (2008). THEMIS observations of long-lived regions of large-amplitude whistler waves in the inner magnetosphere. *Geophysical Research Letters*, *35*, 17. https://doi.org/10.1029/2008GL033643

Demekhov, A. G., Trakhtengerts, V. Y., Rycroft, M., & Nunn, D. (2009). Efficiency of electron acceleration in the Earth's magnetosphere by whistler mode waves. *Geomagnetism and Aeronomy*, *49*(1), 24–29. https://doi.org/10.1134/S0016793209010034

Demekhov, A. G., Trakhtengerts, V. Y., Rycroft, M. J., & Nunn, D. (2006). Electron acceleration in the magnetosphere by whistler-mode waves of varying frequency. *Geomagnetism and Aeronomy*, *46*(6), 711–716. https://doi.org/10.1134/S0016793206060053

Drozdov, A. Y., Shprits, Y. Y., Orlova, K. G., Kellerman, A. C., Subbotin, D. A., Baker, D. N., et al. (2015). Energetic, relativistic, and ultrarelativistic electrons: Comparison of long-term VERB code simulations with Van Allen Probes measurements. *Journal of Geophysical Research*, *120*(5), 3574–3587. https://doi.org/10.1002/2014JA020637

Foster, J. C., Erickson, P. J., Omura, Y., Baker, D. N., Kletzing, C. A., & Claudepierre, S. G. (2017). Van Allen Probes observations of prompt MeV radiation belt electron acceleration in nonlinear interactions with VLF chorus. *Journal of Geophysical Research: Space Physics*, *122*(1), 324–339. https://doi.org/10.1002/2016JA023429

Furuya, N., Omura, Y., & Summers, D. (2008). Relativistic turning acceleration of radiation belt electrons by whistler mode chorus. *Journal of Geophysical Research*, *113*(A4), 4224. https://doi.org/10.1029/2007JA012478

Gan, L., Li, W., Ma, Q., Albert, J. M., Artemyev, A. V., & Bortnik, J. (2020). Nonlinear interactions between radiation belt electrons and chorus waves: Dependence on wave amplitude modulation. *Geophysical Research Letters*, *47*(4), e85987. https://doi.org/10.1029/2019GL085987

Gan, L., Li, W., Ma, Q., Artemyev, A. V., & Albert, J. M. (2020). Unraveling the formation mechanism for the bursts of electron butterfly distributions: Test particle and quasilinear simulations. *Geophysical Research Letters*, *47*(21), e90749. https://doi.org/10.1029/2020GL090749

Gan, L., Li, W., Ma, Q., Artemyev, A. V., & Albert, J. M. (2022). Dependence of nonlinear effects on whistler-mode wave bandwidth and amplitude: A perspective from diffusion coefficients. *Journal of Geophysical Research (Space Physics)*, *127*(5), e30063. https://doi.org/10.1029/2021JA030063

Glauert, S. A., Horne, R. B., & Meredith, N. P. (2018). A 30 year simulation of the outer electron radiation belt. *Journal of Geophysical Research*, *16*(10), 1498–1522. https://doi.org/10.1029/2018SW001981

Grach, V. S., & Demekhov, A. G. (2020). Precipitation of relativistic electrons under resonant interaction with electromagnetic ion cyclotron wave packets. *Journal of Geophysical Research (Space Physics)*, *125*(2), e27358. https://doi.org/10.1029/2019JA027358

Hiraga, R., & Omura, Y. (2020). Acceleration mechanism of radiation belt electrons through interaction with multi-subpacket chorus waves. *Earth Planets and Space*, *72*(1), 21. https://doi.org/10.1186/s40623-020-1134-3

Hsieh, Y.-K., Kubota, Y., & Omura, Y. (2020). Nonlinear evolution of radiation belt electron fluxes interacting with oblique whistler mode chorus emissions. *Journal of Geophysical Research: Space Physics*, *125*(2), e2019JA027465. https://doi.org/10.1029/2019JA027465

Hsieh, Y.-K., & Omura, Y. (2017). Nonlinear dynamics of electrons interacting with oblique whistler mode chorus in the magnetosphere. *Journal of Geophysical Research*, *122*(1), 675–694. https://doi.org/10.1002/2016JA023255

Hsieh, Y.-K., Omura, Y., & Kubota, Y. (2022). Energetic electron precipitation induced by oblique whistler mode chorus emissions. *Journal of Geophysical Research (Space Physics)*, *127*(1), e29583. https://doi.org/10.1029/2021JA029583

Itin, A. P., Neishtadt, A. I., & Vasiliev, A. A. (2000). Captures into resonance and scattering on resonance in dynamics of a charged relativistic particle in magnetic field and electrostatic wave. *Physica D: Nonlinear Phenomena*, *141*(3–4), 281–296. https://doi.org/10.1016/S0167-2789(00)00039-7

Karpman, V. I. (1974). Nonlinear effects in the ELF waves propagating along the magnetic field in the magnetosphere. *Space Science Reviews*, *16*(3), 361–388. https://doi.org/10.1007/BF00171564

Karpman, V. I., Istomin, I. N., & Shkliar, D. R. (1975). Effects of nonlinear interaction of monochromatic waves with resonant particles in the inhomogeneous plasma. *Physica Scripta*, *11*(5), 278–284. https://doi.org/10.1088/0031-8949/11/5/008

Karpman, V. I., Istomin, J. N., & Shklyar, D. R. (1974). Nonlinear theory of a quasi-monochromatic whistler mode packet in inhomogeneous plasma. *Plasma Physics*, *16*(8), 685–703. https://doi.org/10.1088/0032-1028/16/8/001

Karpman, V. I., Istomin, J. N., & Shklyar, D. R. (1975). Particle acceleration by a non-linear Langmuir wave in an inhomogeneous plasma. *Physics Letters A*, *53*(1), 101–102. https://doi.org/10.1016/0375-9601(75)90364-3

Karpman, V. I., & Shklyar, D. R. (1977). Particle precipitation caused by a single whistler-mode wave injected into the magnetosphere. *Planatary Space Science*, *25*(4), 395–403. https://doi.org/10.1016/0032-0633(77)90055-1

Katoh, Y., & Omura, Y. (2007). Relativistic particle acceleration in the process of whistler-mode chorus wave generation. *Geophysical Research Letters*, *34*(13), L13102. https://doi.org/10.1029/2007GL029758

Katoh, Y., & Omura, Y. (2013). Effect of the background magnetic field inhomogeneity on generation processes of whistler-mode chorus and broadband hiss-like emissions. *Journal of Geophysical Research*, *118*(7), 4189–4198. https://doi.org/10.1002/jgra.50395

Katoh, Y., & Omura, Y. (2016). Electron hybrid code simulation of whistler-mode chorus generation with real parameters in the Earth's inner magnetosphere. *Earth Planets and Space*, *68*(1), 192. https://doi.org/10.1186/s40623-016-0568-0

Katoh, Y., Omura, Y., & Summers, D. (2008). Rapid energization of radiation belt electrons by nonlinear wave trapping. *Annales Geophysicae*, *26*(11), 3451–3456. https://doi.org/10.5194/angeo-26-3451-2008

Kennel, C. F., & Engelmann, F. (1966). Velocity space diffusion from weak plasma turbulence in a magnetic field. *Physics of Fluids*, *9*(12), 2377–2388. https://doi.org/10.1063/1.1761629

Kennel, C. F., & Petschek, H. E. (1966). Limit on stably trapped particle fluxes. *Journal of Geophysical Research*, *71*, 1–28. https://doi.org/10.1029/jz071i001p00001

Khazanov, G. V., Tel'nikhin, A. A., & Kronberg, T. K. (2013). Radiation belt electron dynamics driven by large-amplitude whistlers. *Journal of Geophysical Research (Space Physics)*, *118*(10), 6397–6404. https://doi.org/10.1002/2013JA019122

Kletzing, C. A., Kurth, W. S., Acuna, M., MacDowall, R. J., Torbert, R. B., Averkamp, T., et al. (2013). The electric and magnetic field instrument suite and integrated science (EMFISIS) on RBSP. *Space Science Reviews*, *179*(1–4), 127–181. https://doi.org/10.1007/s11214-013-9993-6

Kubota, Y., Omura, Y., & Summers, D. (2015). Relativistic electron precipitation induced by EMIC-triggered emissions in a dipole magnetosphere. *Journal of Geophysical Research (Space Physics)*, *120*(6), 4384–4399. https://doi.org/10.1002/2015JA021017

Le Queau, D., & Roux, A. (1987). Quasi-monochromatic wave-particle interactions in magnetospheric plasmas. *Solar Physics*, *111*(1), 59–80. https://doi.org/10.1007/BF00145441

Li, L., Zhou, X.-Z., Omura, Y., Wang, Z.-H., Zong, Q.-G., Liu, Y., et al. (2018). Nonlinear drift resonance between charged particles and ultralow frequency waves: Theory and observations. *Geophysical Research Letters*, *45*(17), 8773–8782. https://doi.org/10.1029/2018GL079038

Li, L., Zhou, X.-Z., Omura, Y., Zong, Q.-G., Rankin, R., Chen, X.-R., et al. (2021). Drift resonance between particles and compressional toroidal ULF waves in dipole magnetic field. *Journal of Geophysical Research (Space Physics)*, *126*(10), e28842. https://doi.org/10.1029/2020JA028842

Li, W., Bortnik, J., Thorne, R. M., & Angelopoulos, V. (2011). Global distribution of wave amplitudes and wave normal angles of chorus waves using THEMIS wave observations. *Journal of Geophysical Research*, *116*(A12), 12205. https://doi.org/10.1029/2011JA017035

Li, W., & Hudson, M. K. (2019). Earth's Van Allen radiation belts: From discovery to the Van Allen Probes era. *Journal of Geophysical Research (Space Physics)*, *124*(11), 8319–8351. https://doi.org/10.1029/2018JA025940

Li, W., Thorne, R. M., Angelopoulos, V., Bortnik, J., Cully, C. M., Ni, B., et al. (2009). Global distribution of whistler-mode chorus waves observed on the THEMIS spacecraft. *Geophysical Research Letters*, *36*(9), 9104. https://doi.org/10.1029/2009GL037595

Li, W., Thorne, R. M., Ma, Q., Ni, B., Bortnik, J., Baker, D. N., et al. (2014). Radiation belt electron acceleration by chorus waves during the 17 March 2013 storm. *Journal of Geophysical Research*, *119*(6), 4681–4693. https://doi.org/10.1002/2014JA019945

Lukin, A. S., Artemyev, A. V., & Petrukovich, A. A. (2021). On application of stochastic differential equations for simulation of nonlinear wave-particle resonant interactions. *Physics of Plasmas*, *28*(9), 092904. https://doi.org/10.1063/5.0058054

Lyons, L. R., & Williams, D. J. (1984). *Quantitative aspects of magnetospheric physics*. Reidel.

Ma, Q., Li, W., Bortnik, J., Thorne, R. M., Chu, X., Ozeke, L. G., et al. (2018). Quantitative evaluation of radial diffusion and local acceleration processes during GEM challenge events. *Journal of Geophysical Research (Space Physics)*, *123*(3), 1938–1952. https://doi.org/10.1002/2017JA025114

Mauk, B. H., Fox, N. J., Kanekal, S. G., Kessel, R. L., Sibeck, D. G., & Ukhorskiy, A. (2013). Science objectives and rationale for the radiation belt storm probes mission. *Space Science Reviews*, *179*(1–4), 3–27. https://doi.org/10.1007/s11214-012-9908-y

Meredith, N. P., Horne, R. B., Thorne, R. M., & Anderson, R. R. (2003). Favored regions for chorus-driven electron acceleration to relativistic energies in the Earth's outer radiation belt. *Geophysical Research Letters*, *30*(16), 160000-1. https://doi.org/10.1029/2003GL017698

Miyoshi, Y., Hosokawa, S., Kurita, S.-I., Oyama, Y., Ogawa, S., Saito, I., et al. (2021). Penetration of MeV electrons into the mesosphere accompanying pulsating aurorae. *Scientific Reports*, *11*(1), 13724. https://doi.org/10.1038/s41598-021-92611-3

Miyoshi, Y., Saito, S., Kurita, S., Asamura, K., Hosokawa, K., Sakanoi, T., et al. (2020). Relativistic electron microbursts as high-energy tail of pulsating aurora electrons. *Geophysical Research Letters*, *47*(21), e90360. https://doi.org/10.1029/2020GL090360

Mourenas, D., Artemyev, A. V., Agapitov, O. V., & Krasnoselskikh, V. (2014). Consequences of geomagnetic activity on energization and loss of radiation belt electrons by oblique chorus waves. *Journal of Geophysical Research*, *119*(4), 2775–2796. https://doi.org/10.1002/2013JA019674

Mourenas, D., Artemyev, A. V., Agapitov, O. V., Krasnoselskikh, V., & Li, W. (2014). Approximate analytical solutions for the trapped electron distribution due to quasi-linear diffusion by whistler mode waves. *Journal of Geophysical Research*, *119*(12), 9962–9977. https://doi.org/10.1002/2014JA020443

Mourenas, D., Zhang, X.-J., Artemyev, A. V., Angelopoulos, V., Thorne, R. M., Bortnik, J., et al. (2018). Electron nonlinear resonant interaction with short and intense parallel chorus wave packets. *Journal of Geophysical Research*, *123*(6), 4979–4999. https://doi.org/10.1029/2018JA025417

Mourenas, D., Zhang, X. J., Nunn, D., Artemyev, A. V., Angelopoulos, V., Tsai, E., & Wilkins, C. (2022). Short chorus wave packets: Generation within chorus elements, statistics, and consequences on energetic electron precipitation. *Journal of Geophysical Research (Space Physics)*, *127*(5), e30310. https://doi.org/10.1029/2022JA030310

Murphy, K. R., Watt, C. E. J., Mann, I. R., Rae, I. J., Sibeck, D. G., Boyd, A. J., et al. (2018). The global statistical response of the outer radiation belt during geomagnetic storms. *Geophysical Research Letters*, *45*(9), 3783–3792. https://doi.org/10.1002/2017GL076674

Neishtadt, A. I. (1975). Passage through a separatrix in a resonance problem with a slowly-varying parameter. *Journal of Applied Mathematics and Mechanics*, *39*(4), 594–605. https://doi.org/10.1016/0021-8928(75)90060-X

Nunn, D. (1971). Wave-particle interactions in electrostatic waves in an inhomogeneous medium. *Journal of Plasma Physics*, *6*(2), 291–307. https://doi.org/10.1017/S0022377800006061

Nunn, D. (1974). A self-consistent theory of triggered VLF emissions. *Planatary Space Science*, *22*(3), 349–378. https://doi.org/10.1016/0032-0633(74)90070-1

Nunn, D., Zhang, X. J., Mourenas, D., & Artemyev, A. V. (2021). Generation of realistic short chorus wave packets. *Geophysical Research Letters*, *48*(7), e92178. https://doi.org/10.1029/2020GL092178

Omura, Y., Furuya, N., & Summers, D. (2007). Relativistic turning acceleration of resonant electrons by coherent whistler mode waves in a dipole magnetic field. *Journal of Geophysical Research*, *112*(A6), 6236. https://doi.org/10.1029/2006JA012243

Omura, Y., Matsumoto, H., Nunn, D., & Rycroft, M. J. (1991). A review of observational, theoretical and numerical studies of VLF triggered emissions. *Journal of Atmospheric and Terrestrial Physics*, *53*(5), 351–368. https://doi.org/10.1016/0021-9169(91)90031-2

Omura, Y., Miyashita, Y., Yoshikawa, M., Summers, D., Hikishima, M., Ebihara, Y., & Kubota, Y. (2015). Formation process of relativistic electron flux through interaction with chorus emissions in the Earth's inner magnetosphere. *Journal of Geophysical Research*, *120*(11), 9545–9562. https://doi.org/10.1002/2015JA021563

Omura, Y., & Zhao, Q. (2012). Nonlinear pitch angle scattering of relativistic electrons by EMIC waves in the inner magnetosphere. *Journal of Geophysical Research*, *117*(A8), 8227. https://doi.org/10.1029/2012JA017943

Santolík, O., Kletzing, C. A., Kurth, W. S., Hospodarsky, G. B., & Bounds, S. R. (2014). Fine structure of large-amplitude chorus wave packets. *Geophysical Research Letters*, *41*(2), 293–299. https://doi.org/10.1002/2013GL058889

Santolík, O., Parrot, M., & Lefeuvre, F. (2003). Singular value decomposition methods for wave propagation analysis. *Radio Science*, *38*(1), 1010. https://doi.org/10.1029/2000RS002523

Shapiro, V. D., & Sagdeev, R. Z. (1997). Nonlinear wave-particle interaction and conditions for the applicability of quasilinear theory. *Physics Reports*, *283*(1–4), 49–71. https://doi.org/10.1016/S0370-1573(96)00053-1

Shklyar, D. R. (1981). Stochastic motion of relativistic particles in the field of a monochromatic wave. *Soviet Physics Journal of Experimental and Theoretical Physics*, *53*, 1197–1192.

Shklyar, D. R. (2011). On the nature of particle energization via resonant wave-particle interaction in the inhomogeneous magnetospheric plasma. *Annales Geophysicae*, *29*(6), 1179–1188. https://doi.org/10.5194/angeo-29-1179-2011

Shklyar, D. R. (2021). A theory of interaction between relativistic electrons and magnetospherically reflected whistlers. *Journal of Geophysical Research (Space Physics)*, *126*(2), e28799. https://doi.org/10.1029/2020JA028799

Shklyar, D. R., & Matsumoto, H. (2009). Oblique whistler-mode waves in the inhomogeneous magnetospheric plasma: Resonant interactions with energetic charged particles. *Surveys in Geophysics*, *30*(2), 55–104. https://doi.org/10.1007/s10712-009-9061-7

Stix, T. H. (1962). *The theory of plasma waves*. McGraw-Hill Book Company, Inc.

Su, Z., Gao, Z., Zhu, H., Li, W., Zheng, H., Wang, Y., et al. (2016). Nonstorm time dropout of radiation belt electron fluxes on 24 September 2013. *Journal of Geophysical Research*, *121*(7), 6400–6416. https://doi.org/10.1002/2016JA022546

Summers, D., & Omura, Y. (2007). Ultra-relativistic acceleration of electrons in planetary magnetospheres. *Geophysical Research Letters*, *34*(24), 24205. https://doi.org/10.1029/2007GL032226

Tao, X., Bortnik, J., Albert, J. M., & Thorne, R. M. (2012). Comparison of bounce-averaged quasi-linear diffusion coefficients for parallel propagating whistler mode waves with test particle simulations. *Journal of Geophysical Research*, *117*(A10), 10205. https://doi.org/10.1029/2012JA017931

Tao, X., Bortnik, J., Albert, J. M., Thorne, R. M., & Li, W. (2013). The importance of amplitude modulation in nonlinear interactions between electrons and large amplitude whistler waves. *Journal of Atmospheric and Solar-Terrestrial Physics*, *99*, 67–72. https://doi.org/10.1016/j.jastp.2012.05.012

Tao, X., Zonca, F., & Chen, L. (2017). Identify the nonlinear wave-particle interaction regime in rising tone chorus generation. *Geophysical Research Letters*, *44*(8), 3441–3446. https://doi.org/10.1002/2017GL072624

Thorne, R. M., Li, W., Ni, B., Ma, Q., Bortnik, J., Chen, L., et al. (2013). Rapid local acceleration of relativistic radiation-belt electrons by magnetospheric chorus. *Nature*, *504*(7480), 411–414. https://doi.org/10.1038/nature12889

Tsai, E., Artemyev, A., Zhang, X.-J., & Angelopoulos, V. (2022). Relativistic electron precipitation driven by nonlinear resonance with whistler-mode waves. *Journal of Geophysical Research (Space Physics)*, *127*(5), e30338. https://doi.org/10.1029/2022JA030338

Tu, W., Cunningham, G. S., Chen, Y., Morley, S. K., Reeves, G. D., Blake, J. B., et al. (2014). Event-specific chorus wave and electron seed population models in DREAM3D using the Van Allen Probes. *Geophysical Research Letters*, *41*(5), 1359–1366. https://doi.org/10.1002/2013GL058819

Tyler, E., Breneman, A., Cattell, C., Wygant, J., Thaller, S., & Malaspina, D. (2019). Statistical occurrence and distribution of high-amplitude whistler mode waves in the outer radiation belt. *Geophysical Research Letters*, *46*(5), 2328–2336. https://doi.org/10.1029/2019GL082292

Vainchtein, D., Zhang, X. J., Artemyev, A. V., Mourenas, D., Angelopoulos, V., & Thorne, R. M. (2018). Evolution of electron distribution driven by nonlinear resonances with intense field-aligned chorus waves. *Journal of Geophysical Research (Space Physics)*, *123*(10), 8149–8169. https://doi.org/10.1029/2018JA025654

Vedenov, A. A., Velikhov, E., & Sagdeev, R. (1962). Quasilinear theory of plasma oscillations. *Nuclear Fusion Supplement*, *2*, 465–475.

Wang, D., Shprits, Y. Y., Zhelavskaya, I. S., Agapitov, O. V., Drozdov, A. Y., & Aseev, N. A. (2019). Analytical chorus wave model derived from Van Allen Probe observations. *Journal of Geophysical Research (Space Physics)*, *124*(2), 1063–1084. https://doi.org/10.1029/2018JA026183

Wilson, L. B., III, Cattell, C. A., Kellogg, P. J., Wygant, J. R., Goetz, K., Breneman, A., & Kersten, K. (2011). The properties of large amplitude whistler mode waves in the magnetosphere: Propagation and relationship with geomagnetic activity. *Geophysical Research Letters*, *38*(17), 17107. https://doi.org/10.1029/2011GL048671

Zhang, X. J., Agapitov, O., Artemyev, A. V., Mourenas, D., Angelopoulos, V., Kurth, W. S., et al. (2020). Phase decoherence within intense chorus wave packets constrains the efficiency of nonlinear resonant electron acceleration. *Geophysical Research Letters*, *47*(20), e89807. https://doi.org/10.1029/2020GL089807

Zhang, X.-J., Angelopoulos, V., Mourenas, D., Artemyev, A. V., Tsai, E., & Wilkins, C. (2022). Characteristics of electron microburst precipitation based on high-resolution ELFIN measurements. *Journal of Geophysical Research*, *127*(5), e2022JA030509. https://doi.org/10.1029/2022JA030509

Zhang, X.-J., Artemyev, A., Angelopoulos, V., Tsai, E., Wilkins, C., Kasahara, S., et al. (2022). Superfast precipitation of energetic electrons in the radiation belts of the Earth. *Nature Communications*, *13*(1), 1611. https://doi.org/10.1038/s41467-022-29291-8

Zhang, X. J., Demekhov, A. G., Katoh, Y., Nunn, D., Tao, X., Mourenas, D., et al. (2021). Fine structure of chorus wave packets: Comparison between observations and wave generation models. *Journal of Geophysical Research (Space Physics)*, *126*(8), e29330. https://doi.org/10.1029/2021JA029330

Zhang, X. J., Mourenas, D., Artemyev, A. V., Angelopoulos, V., Bortnik, J., Thorne, R. M., et al. (2019). Nonlinear electron interaction with intense chorus waves: Statistics of occurrence rates. *Geophysical Research Letters*, *46*(13), 7182–7190. https://doi.org/10.1029/2019GL083833

Zhang, X. J., Mourenas, D., Artemyev, A. V., Angelopoulos, V., Kurth, W. S., Kletzing, C. A., & Hospodarsky, G. B. (2020). Rapid frequency variations within intense chorus wave packets. *Geophysical Research Letters*, *47*(15), e88853. https://doi.org/10.1029/2020GL088853

Zhang, X. J., Thorne, R., Artemyev, A., Mourenas, D., Angelopoulos, V., Bortnik, J., et al. (2018). Properties of intense field-aligned lower-band chorus waves: Implications for nonlinear wave-particle interactions. *Journal of Geophysical Research (Space Physics)*, *123*(7), 5379–5393. https://doi.org/10.1029/2018JA025390